recycling

MDPI

*Article*

# Apple Pruning-Derived Activated Biochar and Hydrochar for Efficient Dye Adsorption: Response Surface Methodology-Guided Optimization, Kinetic Analysis, and Mechanistic Modelling

**Ameni Ben Salah [1], M. Mirari Antxustegi [1], Eriz Corro [1] and María González Alriols [2,*]**

[1] Biorefinery Processes Research Group (BioRP), Chemical and Environmental Engineering Department, University of the Basque Country (UPV/EHU), Avda. Otaola 29, 20600 Eibar, Gipuzkoa, Spain; ameni.bensalah@ehu.eus (A.B.S.); mirari.antxustegi@ehu.eus (M.M.A.); eriz.corro@ehu.eus (E.C.)

[2] Biorefinery Processes Research Group (BioRP), Chemical and Environmental Engineering Department, University of the Basque Country (UPV/EHU), Plaza Europa 1, 20018 San Sebastian, Gipuzkoa, Spain

* Correspondence: maria.gonzalez@ehu.eus

**Abstract**

This study explores the valorisation of apple pruning (AP) residues into sustainable carbonaceous adsorbents for dye-contaminated wastewater. Activated biochars (ABCs) were produced via single-step (ABC-1S) and two-step (ABC-2S) KOH activation, while activated hydrochar (AHTC) was obtained through hydrothermal carbonization followed by $H_3PO_4$ activation. The materials were comprehensively characterized using proximate analysis, FTIR spectroscopy, SEM imaging, and $N_2$ adsorption–desorption to evaluate surface chemistry, morphology, and textural properties. Batch adsorption experiments using MB (5–100 mg/L) demonstrated the superior performance of ABCs compared to AHTC. At low dye concentrations, adsorption on ABCs was partially influenced by external mass transfer, while kinetic data were best described by the Avrami model, indicating complex adsorption mechanisms. Isotherm analysis showed that ABC-2S exhibited heterogeneous adsorption behaviour, whereas AHTC poorly conformed to conventional isotherm models. The Langmuir model indicated higher monolayer capacities for ABCs (up to 22.9 mg/g) relative to AHTC (9.7 mg/g), reflecting a greater density of accessible adsorption sites induced by alkaline activation. Notably, nearly complete methylene blue (MB) removal was maintained over three regeneration cycles, confirming the stability, reusability, and practical potential of AP-derived ABCs and AHTC for sustainable wastewater treatment.

**Keywords:** activated biochar; adsorption isotherms; adsorption kinetics; apple pruning waste; hydrochar; methylene blue; response surface methodology (RSM); removal efficiency

Check for updates

Academic Editor: Francesco Ferella

Received: 31 December 2025
Revised: 4 February 2026
Accepted: 7 February 2026
Published: 4 March 2026

**Copyright:** © 2026 by the authors. Licensee MDPI, Basel, Switzerland. This article is an open access article distributed under the terms and conditions of the Creative Commons Attribution (CC BY) license.

## 1. Introduction

Water pollution is increasingly recognized as a major global environmental threat, largely driven by industrial expansion and rising population, which together intensify wastewater generation [1]. Among the sectors contributing most to this problem, the textile industry stands out for releasing large volumes of dye-containing effluents that accumulate persistently in aquatic systems [2]. Textile dye effluents present considerable ecological and human health hazards due to the persistence and degradation resistance of synthetic dyes in natural environments, frequently resulting in prolonged contamination of aquatic systems [3]. Approximately 10–15% of dyes utilized in textile manufacturing

do not adhere to fabrics and are released into wastewater, resulting in significant contamination and pronounced coloration of aquatic habitats [4]. This pronounced pigmentation diminishes light penetration and hinders photosynthesis in aquatic vegetation, resulting in decreased dissolved oxygen levels and disrupting aquatic food webs [5]. Numerous dye compounds and their breakdown products demonstrate hazardous, mutagenic, and carcinogenic properties, potentially affecting fish, invertebrates, and human health via direct exposure or bioaccumulation [6]. In humans, contact with dye-contaminated water has been associated with dermal irritation, respiratory complications, organ damage, and an elevated risk of cancer, especially with prolonged exposure [7] Overall, recent comprehensive assessments underscore that dye pollution is a significant environmental concern linked to industrial wastewater and stress the urgent necessity for effective and sustainable remediation strategies [8]. These dyes often coexist with additional hazardous pollutants such as heavy metals and phenolic compounds, reinforcing the need for efficient and sustainable treatment methods [9].

Although several advanced technologies have been proposed for wastewater purification, adsorption has emerged as one of the most effective and economically viable options due to its simplicity, adaptability, and high removal efficiency [10]. Conventional activated carbon is known for its excellent adsorptive performance, but its elevated production cost drives the search for renewable and low-cost alternatives [11]. Biomass-derived carbonaceous materials, particularly biochar (BC) and hydrochar (HTC), are gaining interest because they are abundant, structurally tunable, and environmentally sustainable [12].

BC is produced by pyrolysis under oxygen-limited conditions, yielding amaterial with high surface area and reactive functional groups that can vary depending on the feedstock and process temperature [13]. HTC, by contrast, is obtained through hydrothermal carbonization, which converts biomass into a carbon-rich solid under moderate temperatures and self-generated pressure in a water-based reaction environment [14]. HTCs typically contain abundant oxygenated functional groups, making them suitable materials for pollutant adsorption [15]. However, agro-residue-based BCs and HTCs often show limited surface area and structural stability, which can restrict their performance [10]. However, agro-residue -based BCs and HTCs often show limited surface area and structural stability, which can restrict their performance [16]. To mitigate these limitations, chemical activation has proven an effective strategy to create porosity, increase surface area, and promote stronger interactions between adsorbent and pollutant molecules [17]. These enhancements are particularly advantageous for chemical adsorption processes, where the formation of stable covalent or ionic bonds plays a central role [18].

Agricultural residues from apple production represent an attractive biomass source for adsorbent preparation. In northern Spain, and specifically in the Gipuzkoa region, apple cultivation generates substantial residual annual biomass (apple pruning, AP), offering both a waste management solution and an opportunity to create value-added carbon materials [19].

In this study, activated biochars (ABCs) and hydrochar (AHTC) were synthesized from AP to assess their performance in removing methylene blue (MB) from aqueous solutions. ABCs were produced by two different schemes: a one-step (1S) route based on a simultaneous thermochemical and activation process, and a two-step (2S) one, with sequential thermochemical and activation stages. In both schemes, the thermochemical process was conducted at 900 °C, above conventional pyrolysis temperatures to enhance carbon structural consolidation and explore the resulting impact on material stability [20]. Hydrothermal treatment was performed at 200 °C for 24 h, followed by chemical activation with $H_3PO_4$, conditions associated with structural dehydration and the development of porosity through phosphate decomposition [21].

The strength of this work lies in its comprehensive mechanistic assessment. The materials were characterized using ATR-FTIR to analyse surface chemistry [15], SEM to investigate morphology [14], and NLDFT to determine surface area and pore structure [16]. Adsorption kinetics were examined through multiple non-linear models to identify rate-controlling steps and diffusion mechanisms, while adsorption isotherms were evaluated using a diverse set of equilibrium models to provide deeper insight into adsorption capacity and surface heterogeneity [22].

Finally, the reusability of adsorbents was assessed over three adsorption–desorption cycles using acetone as the desorbing agent. MB removal remained consistently high across all cycles, demonstrating excellent structural stability and regeneration efficiency, and highlighting the potential of these materials for real wastewater treatment applications [20].

## 2. Results and Discussion

### *2.1. Characterization of Adsorbents*

#### 2.1.1. Proximate and Ultimate Analysis

The results obtained from the proximate and ultimate analyses of the biomass precursor and the ABCs and AHTC samples are shown in Table 1. The activated material shows significant carbon enrichment compared to AP (45% C), the activation process indicates more condensed aromatic/graphitic structure (C–C/C=C) [9] that improves π–π interactions with organic pollutants (dyes, phenols, pharmaceuticals) [18]. The extremely low H/C ratio in HTC (0.005) and the low O/C ratio refer to hydrophobicity and high long-term stability [23]. These factors impact the performance to absorb polar and non-polar contaminants and lipophilic organic compounds, like MB, during repeated adsorption cycles [24]. ABC-1S and AHTC still contain some nitrogen (0.40 and 0.56 dry basis, wt.%) while ABC-2S does not. Activation at higher temperatures (900 °C) promotes decomposition and volatilisation of heteroatom species (e.g., N-functional groups), resulting in a carbon matrix with negligible (ABC-2S) or low (ABC-1S) nitrogen content compared to AHTC, which was treated at lower temperatures (450 °C) [24]. In addition, sulfur was effectively incorporated, with its content reaching up to 2.6% for AHTC. This increases the surface basicity, attracting cationic MB and enhancing charge transfer [25]. Meanwhile, the sulphur groups provide polarizable sites and promote MB adsorption through soft-acid soft-base interactions [26].

**Table 1.** Proximate and ultimate analysis (dry basis, wt.%) of AP and adsorbents (ABC-1S, ABC-2S and AHTC).

| Analysis | Parameter | AP | ABC-1S | ABC-2S | AHTC |
|---|---|---|---|---|---|
| Proximate analysis (wt.%) | Fixed carbon (%) | 14.86 | - | - | - |
| | Volatile matter (%) | 79.69 | - | - | - |
| | Inorganic matter (%) | 5.45 | - | - | - |
| | Moisture (%) | 8.68 | - | - | - |
| Ultimate analysis (wt.%, ash free) | C (%) | 45.04 | 85.05 | 74.87 | 76.67 |
| | H (%) | 5.71 | - | - | 0.38 |
| | N (%) | 0.73 | 0.40 | - | 0.56 |
| | S (%) | 0.72 | 0.11 | 0.48 | 2.60 |
| | O (%) | 42.35 | 14.44 | 24.65 | 19.79 |
| | O/C | 0.94 | 0.17 | 0.33 | 0.26 |
| | H/C | 0.13 | - | - | 0.005 |

#### 2.1.2. Pore Structure of the Adsorbents

The $N_2$ adsorption/desorption isotherms shown in Figure 1a for ABC-1S and ABC-2S demonstrate a swift rise in adsorbed volume at low relative pressures, subsequently

followed by a hysteresis loop at higher relative pressures. This observation signifies the coexistence of micropores and mesopores, a common feature of ABCs. The presence of such Type IV profiles with hysteresis has been documented in the literature as a hallmark of hierarchical pore structures in mesoporous carbon materials and ABCs, which exhibit an integration of high surface area with capillary condensation effects in mesopores [27].

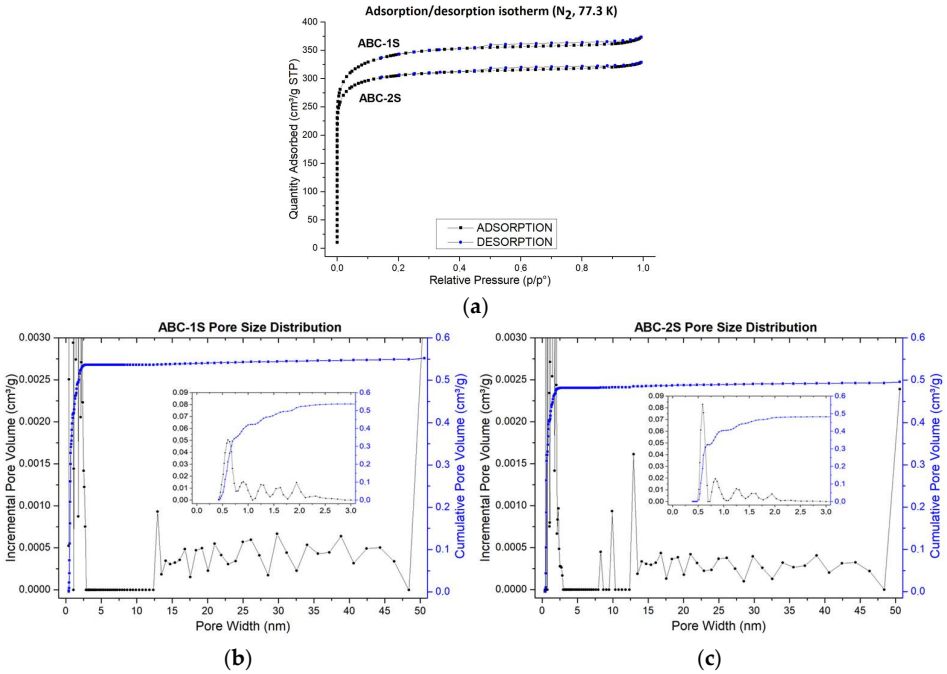
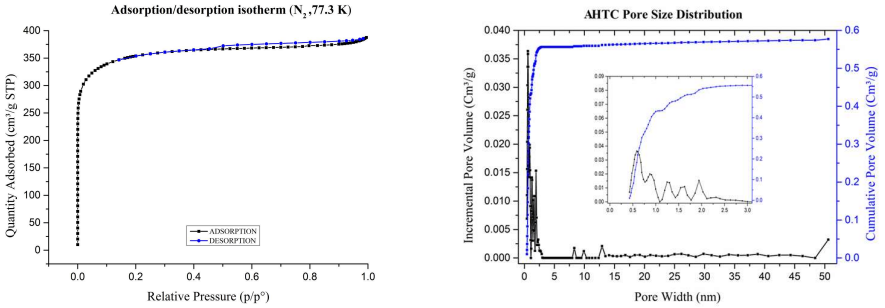



**Figure 1.** $N_2$ adsorption/desorption isotherms (**a**) and calculated (NDFT) pore size distribution curves of ABC-1S (**b**) and ABC-2S (**c**).

The pore size distribution data, Figure 1b,c reveal the presence of dominant micropore peaks (<2 nm) in addition to features in the 2–10 nm range, thus confirming a mixed pore structure. This finding is in accordance with recent research, which demonstrates that effective activation strategies result in ABCs with concentrated microporosity and a high surface area, in conjunction with secondary mesopores that facilitate faster diffusion and capillary condensation [27]. ABC-1S sample's mesoporous structure begins with pores at the lower end of the mesoporous range (around 2 nm), followed by a broad distribution with pronounced features between 12 and 40 nm, with the main maximum centred at 12 nm. In contrast, the ABC-2S sample showed its most intense pore size contributions in the 10–14 nm region, accompanied by a residual porosity extending up to 50 nm.

The $N_2$ adsorption/desorption of AHTC, Figure 2a, displays a characteristic Type I behaviour, exhibiting a pronounced nitrogen uptake at low relative pressures ($p/p_0 < 0.1$). This observation signifies a micropore-dominated structure and constrained mesoporosity, which is a hallmark of carbons subjected to chemical activation with $H_3PO_4$ [28]. The plateau observed at higher relative pressures provides further confirmation that adsorption is primarily governed by micropore filling rather than mesopore capillary condensation.

The pore size distribution, Figure 2b, provides support for this observation, indicating that most of the pore volume is concentrated in the micropore region (<2 nm). This finding is consistent with the literature on phosphoric acid-AHTCs, where narrow pore formation is commonly reported to be promoted by dehydration and cross-linking reactions during activation [29]. It has been demonstrated that a microporous structure is associated with enhanced adsorption performance towards small molecules, such as MB. This enhanced performance is understood to result from a combination of factors, including π–π interactions, electrostatic attraction, and hydrogen bonding [30].




(**a**) (**b**)

**Figure 2.** $N_2$ adsorption/desorption isotherms (**a**) and calculated (NDFT) pore size distribution curves of AHTC (**b**).

A summary of the porosity and surface properties is presented in Table 2, where a strong influence of the activating agent on pore development and adsorption behaviour can be observed. ABC-1S and ABC-2S exhibit a highly developed microporous structure with average pore widths of 1.753 and 1.709 nm, respectively, as well as extremely high microporous surface areas of 1425.5 and 1305.6 $m^2/g$. This strongly suggests that micropore formation is the dominant effect of KOH activation. This extensive microporosity is the key parameter responsible for their high adsorption potential, as adsorption in such materials is primarily governed by micropore filling.

**Table 2.** Porosity and textural properties.

| Sample | $S_{BET}$ ($m^2/g$) | $S_{tot}$ ($m^2/g$) | $S_{micro}$ ($m^2/g$) | $S_{meso}$ ($m^2/g$) | $V_{tot}$ ($cm^3/g$) | $V_{micro}$ ($cm^3/g$) | $V_{meso}$ ($cm^3/g$) | Average Pore Width (nm) |
|---|---|---|---|---|---|---|---|---|
| ABC-1S | 1297.2 | 1480.1 | 1425.5 | 54.61 | 0.5523 | 0.5066 | 0.0457 | 1.753 |
| ABC-2S | 1176.2 | 1401.5 | 1305.6 | 95.93 | 0.4960 | 0.4640 | 0.0320 | 1.709 |
| AHTC | 1342.8 | 1528.6 | 1453.6 | 75.00 | 0.5771 | 0.5166 | 0.0605 | 1.761 |

Where $S_{BET}$: BET specific surface area; $S_{tot}/V_{tot}$: total pore surface/ volume obtained using 2D-NLDFT models; $S_{micro}/V_{micro}$: Surface and volume of micropores using Dubinin-Radushkevich models; $S_{meso}/V_{meso}$: The mesopore surface/volume was determined by subtracting $S_{micro}$ and $V_{micro}$ from $S_{tot}$ and $V_{tot}$, respectively.

Nitrogen adsorption in microporous materials proceeds predominantly through pore-filling mechanisms rather than multilayer adsorption, which leads the BET model to systematically underestimate surface area in highly microporous systems. In contrast, Dubinin–Radushkevich (DR) analysis more accurately accounts for micropore filling phenomena, thereby providing a more reliable estimation of microporous contributions. These discrepancies between BET-derived and DR-derived surface areas have been extensively discussed in the literature for a wide range of microporous and mesoporous adsorbents, underscoring the importance of using complementary characterization methods [31].

To obtain a more comprehensive textural assessment, the total surface area (Stot) and total pore volume were derived from nitrogen adsorption isotherms using 2D-NLDFT models, which offer enhanced resolution of micro- and mesopore structures compared with traditional BET analysis. The 2D-NLDFT framework incorporates pore geometry, adsorbate–adsorbent interactions, and surface heterogeneity, enabling more robust and physically realistic characterization of porous carbons [32].

ABC-1S has a higher microporous surface area and pore volume than ABC-2S, suggesting a greater density of accessible adsorption sites. In contrast, AHTC exhibits the highest overall $S_{BET}$ (1342.8 $m^2/g$) and total pore volume (0.5771 $cm^3/g$), as well as the largest mesoporous contribution ($V_{meso}$ = 0.0605 $cm^3/g$). This reflects the ability of phosphoric acid activation to generate a hierarchical micro-mesoporous structure.

While AHTC remains microporous ($S_{micro}$ = 1453.6 $m^2/g$; pore width = 1.781 nm), Mesopores improve mass transfer and micropore access, enhancing adsorption kinetics. Key structural parameters for adsorption capacity include microporous surface area, micropore volume, narrow pore width, and activating agent influence.

### 2.1.3. ATR-FTIR Analysis

The FTIR spectra in Figure 3 reveal several shared functional groups characterized by specific wavenumbers. Both AHTC and ABC-2S show strong aliphatic bond at 2981 $cm^{-1}$ and 2896 $cm^{-1}$ [16], corresponding to asymmetric and symmetric [33] $sp^3$ C–H [34] stretching vibrations of alkyl group [35] such as methyl and methylene groups [36], along with overlapping O–H stretching from carboxylic acids [34]. The aliphatic groups mostly contribute to hydrophobic and van der Waals interactions, enhancing surface heterogeneity and promoting pore diffusion and molecular access, in accordance with findings in modified materials utilized for MB adsorption [37].

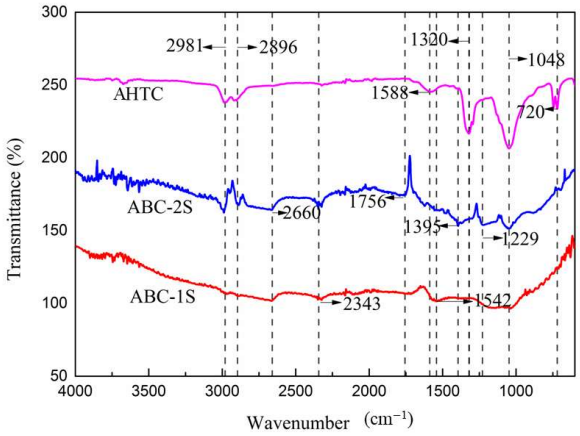



**Figure 3.** ATR-FTIR spectra of APBC-1S, APBC-2S and AHTC.

The peak at 2343 $cm^{-1}$ observed in ABC-1S and ABC-2S is attributed to C=O stretching from atmospheric $CO_2$ [38] and amide groups [39]. At 1756 $cm^{-1}$, ABC-2S exhibits C=O stretching linked to carboxyl, lactone [34], ester, ketone, and aldehyde groups [35] which offer active sites for electrostatic attraction, hydrogen bonding and surface complexation with cationic MB [21].

Aromatic skeletal vibrations (C=C stretch) [16] and C=N bonds [40] are noted at 1588 $cm^{-1}$ in AHTC and 1542 $cm^{-1}$ in ABC-1S, indicating aromatic ring structures [41]. Those groups are crucial for π–π stacking and π–π electron-donor–acceptor (EDA) interactions with the aromatic rings of MB, thereby enhancing affinity and chemisorption strength [42].

Additionally, bending vibrations such as C–H $sp^3$ bending [9] and O–H bending for methyl symmetric deformation [41] occur around 1395 $cm^{-1}$ in ABC-2S. C–O stretching vibrations, related to lignin, cellulose, acyl, phenol, and alcohol groups [41], appear prominently at 1320 $cm^{-1}$ of methyl symmetric deformation of $CH_3$ Group [40], 1229 $cm^{-1}$, and 1048 $cm^{-1}$ across the samples are promoting hydrogen bonding and increase surface polarity which enable N–π interactions by having lone-pair electrons interact with the aromatic system of MB [43]. Lastly, AHTC shows a distinct C–OH out-of-plane bending at 720 $cm^{-1}$ [41]. Overall, functional groups enhance surface heterogeneity, promoting strong chemisorption (electrostatic attraction, hydrogen bonding, surface complexation) and weaker physisorption (π–π interactions, van der Waals forces, pore filling) in adsorbents for MB removal [44].

2.1.4. Scanning Electron Microscopy (SEM)

The SEM micrographs of the three materials (Figure 4) reveal clear morphological distinctions that reflect their different synthesis routes and directly influence their adsorption behaviour.

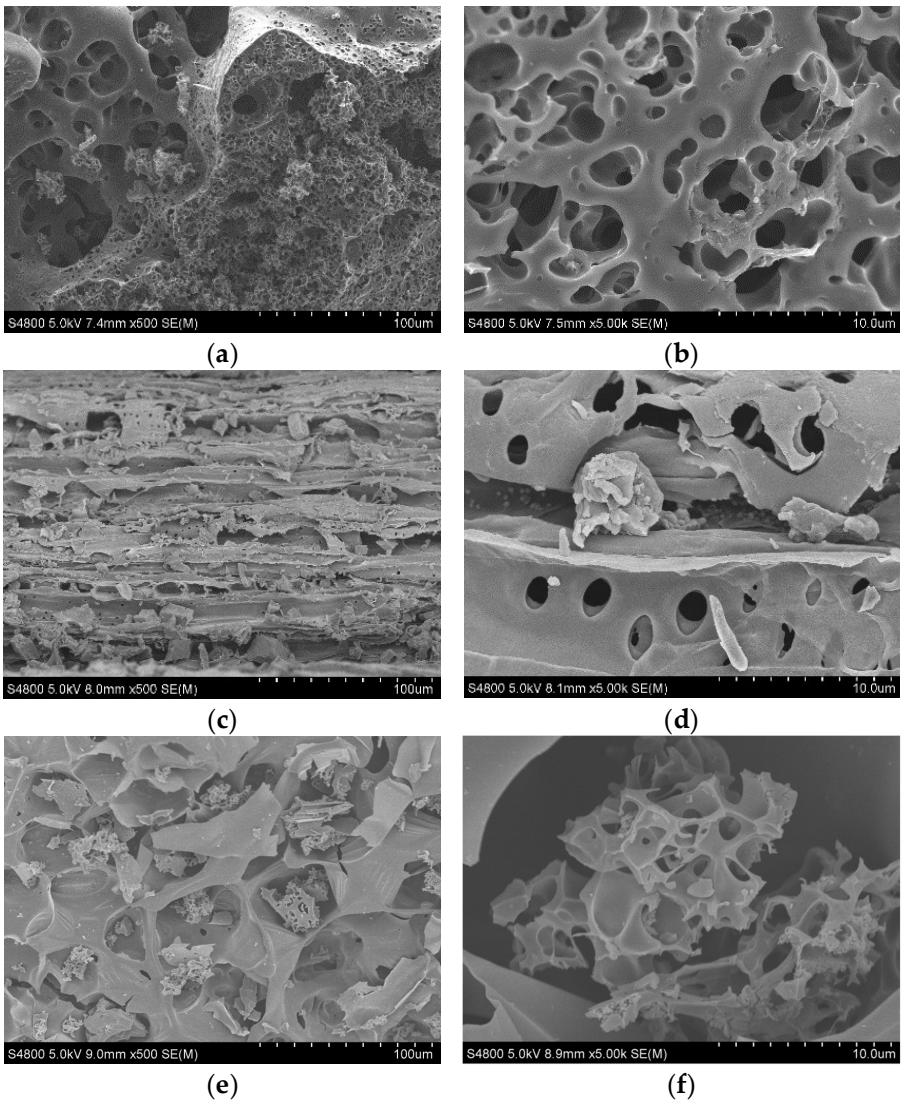



**Figure 4.** SEM images of ABC-1S (**a**,**b**), ABC-2S (**c**,**d**) and AHTC (**e**,**f**).

Both ABC-1S and ABC-2S display the characteristic features of high-temperature pyrolyzed biochars, including a rigid and fractured carbon matrix with irregular cavities and open mesoporous structures generated by extensive devolatilization and carbon restructuring at 900 °C. ABC-1S' images, Figure 4a,b, manifest a polished and compact surface with minimal visible pores, which is consistent with the concurrent pyrolysis/KOH activation process [45], in which rapid devolatilisation and vigorous KOH-carbon reactions can result in the fusion of surface layers or the collapse of pore channels [45,46],. Recent mechanistic studies have indicated that the activation of KOH results in the generation of porosity through redox and gasification pathways ($KOH \rightarrow K_2O/K \rightarrow K_2CO_3 + CO/CO_2$). Moreover, it has been observed that the application of excessive activation conditions leads to an increase in structural damage [47]. In contrast, the ABC-2S sample Figure 4c,d exhibits a rough, irregular surface with numerous small pores, while also preserving fragments of the original biomass cellular structure. This morphology has been previously reported for 2-S KOH activation, where controlled chemical etching leads to the development of

micro/mesopores without fully collapsing the precursor framework [46]. AHTC sample Figure 4e,f, produced via hydrothermal carbonization followed by $H_3PO_4$ activation, retains the smoother, rounded morphology typical of hydrochar-derived materials. Its surface appears more compact, composed of aggregated spherical or bead-like structures, and although activation introduces porosity, the resulting texture is more uniform and less fractured than that of the ABC samples. These morphological differences imply that the ABC materials provide greater external pore accessibility and more efficient diffusion pathways due to their open fissures and broader mesoporous structures, while AHTC's more compact and chemically etched surface likely favours interactions driven by surface functionalities rather than extensive external porosity. Together, the SEM observations show that ABC-type adsorbents possess a more open and accessible morphology conducive to rapid mass transfer, whereas AHTC offers a chemically functional but less externally porous architecture, explaining the performance differences observed between the materials.

### *2.2. Adsorption Studies*

#### 2.2.1. 3D Response Surface for MB Removal

The coefficients of the quadratic models for ABC-1S, ABC-2S, and AHTC generated through RSM are listed in Table 3, where ABC-1S and ABC-2S have higher intercept ($\beta_0$) values than AHTC, showing their better MB removal capability. This is due to their greater microporosity and higher surface area created by KOH activation [48]. ABC-1S shows improved adsorption with higher activation severity, while ABC-2S's negative linear coefficient suggests KOH activation leading to pore widening or collapse, as seen with alkali-ABCs. Small interaction terms and negative quadratic coefficients show limited synergistic effects, confirming an optimum adsorption region consistent with RSM studies on KOH-ABCs.

**Table 3.** Regression coefficients of the quadratic RSM models for ABC-1S, ABC-2S and AHTC.

| Coefficient | ABC-1S | ABC-2S | AHTC |
|---|---|---|---|
| $\beta_0$ | 62.38 | 50.12 | 25.39 |
| $\beta_1$ | 0.19 | −0.60 | 0.04 |
| $\beta_2$ | 0.07 | 0.1 | 0.0563 |
| $\beta_{12}$ | 0.0004 | 0.0004 | 0.0001 |
| $\beta_{11}$ | −0.0046 | 0.0019 | −0.0011 |
| $\beta_{22}$ | $-4.24 \times 10^{-5}$ | $-5.077 \times 10^{-5}$ | $-1.607 \times 10^{-5}$ |

As demonstrated in Table 4, the key model fit statistics, including $R^2$, adjusted $R^2$, AIC, and BIC, are presented. The high $R^2$ and adjusted $R^2$ values for ABC-2S demonstrate excellent agreement between experimental and predicted MB removal, reflecting the homogeneous pore structure and strong dependence on operating variables, which are typical of KOH-ABCs optimised by RSM. In contrast, the lower $R^2$ values for ABC-1S and AHTC indicate greater heterogeneity and weaker model predictability.

**Table 4.** Fit Statistics of the Quadratic Models for MB Removal.

| Sample | $R^2$ | Adjusted $R^2$ | AIC | BIC |
|---|---|---|---|---|
| ABC-1S | 0.5611 | 0.5568 | 3928.83 | 3954 |
| ABC-2S | 0.8677 | 0.8664 | 3524.29 | 3550 |
| AHTC | 0.4987 | 0.4937 | 4254.68 | 4279 |

Where AIC and BIC are respectively Akaike Information Criterion and Bayesian Information Criterion [49], those two statistical model-selection tools evaluate model adequacy by balancing goodness of fit with model complexity [50].

The removal efficiency curves for MB Figure 5 for ABC-1S (a), ABC-2S (c) and AHTC (e), demonstrate a rapid increase in percentage removal at early contact times, followed by a slower approach to equilibrium. This pattern is commonly observed in MB adsorption due to the abundance of available active sites initially, and their progressive occupation with time. This has been reported in many MB adsorption studies. Efficiency increases quickly at the start because surface sites are available, and then gradually plateaus as sites become occupied and mass transfer limitations take over [51]. Higher concentrations typically result in lower removal rates at a fixed time due to competition for adsorption sites and take longer to reach high removal levels, as shown in graphs [15].

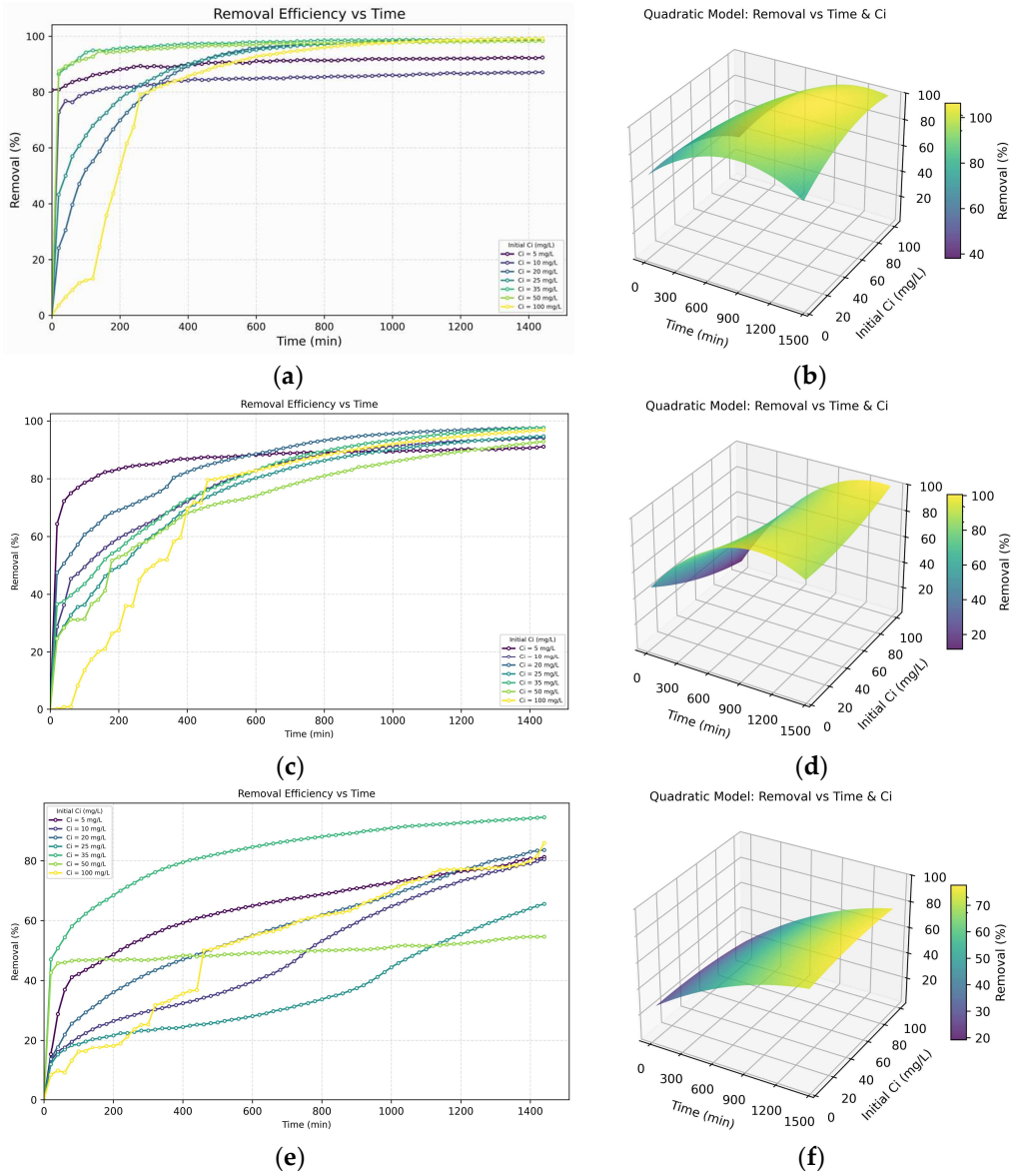



**Figure 5.** Removal efficiency f and the RSM quadratic model for: ABC-1S (**a**,**b**), ABC-2S (**c**,**d**) and AHTC (**e**,**f**).

The RSM 3D surface plots indicate that MB removal escalates with both contact duration and initial dye concentration, paralleling results from other RSM investigations where prolonged contact time and optimized parameters markedly improved MB adsorption [52].

Figure 5 ABC-1S (b), and particularly ABC-2S (d), exhibit more pronounced surfaces and enhanced removal efficiencies, indicating more robust interactions and superior adsorption kinetics, similar to the significant removal and strong quadratic model fits documented for carboxymethyl cellulose–based hydrogel beads optimized through RSM-BBD for MB removal [51]. In comparison, the AHTC surface displays Figure 5f a more gradual increase in removal with time and Ci, corresponding with prior AHTC RSM investigations where ideal conditions still required careful management of factors to attain high efficiencies [53]. These comparisons highlight the significance of contact time and initial concentration as critical parameters in RSM models for dye adsorption.

#### 2.2.2. Kinetic Study

The results of the kinetic fitting reveal different ways in which MB is adsorbed depending on the type of material and how it is activated. For ABC-1S and ABC-2S Figures 6 and 7, adsorption at low concentrations is partly determined by external mass transfer, as shown by the high liquid film diffusion fits for ABC-1S at 5 mg/L ($R^2$ = 0.949), Figure 6f and ABC-2S at 10–25 mg/L ($R^2 \approx 0.96$–$0.98$), Figure 7f, which is commonly reported for highly porous ABCs at low driving forces [54]. At intermediate concentrations (10–50 mg/L), both ABC-1S and ABC-2S are best described by the Avrami model, Figures 6e and 7e, ($R^2$ = 0.996–1.000), in conjunction with strong Elovich, Figures 6c and 7c, and Bangham fits, Figures 6g and 7g. This finding indicates heterogeneous chemisorption and pore-controlled uptake, a conclusion that is consistent with recent Avrami-based analyses of MB adsorption on ABCs with non-uniform energy sites [55]. In contrast, AHTC (Figure 8) demonstrates consistently high Elovich, Figure 8c, Bangham, Figure 8g, and Weber–Morris, Figure 8h, fits across most concentrations (e.g., $R^2$ = 0.993–0.996 at 5–35 mg/L), suggesting that adsorption is dominated by surface heterogeneity and intra-particle diffusion rather than strong chemisorption. This behaviour has been widely observed for AHTCs with lower graphitisation and higher oxygen functionality [56].

In short, KOH activation promotes the uptake of MB by chemisorption, while phosphoric-acid-AHTC exhibits diffusion-dominated heterogeneous adsorption. This agrees with recent ABC–AHTCs dye adsorption studies.

The adsorption kinetics of MB onto both ABC-1S Tables 5 and 6 and ABC-2S demonstrate a process dominated by chemisorption and surface interactions modulated by diffusion phenomena. The equilibrium capacities ($q_e$) from the PSO model exhibited an increase with initial MB concentration, with PSO $q_e$ ranging from ~0.75 to ~19.79 mg/g for ABC-1S and ~0.74 to ~11.71 mg/g for ABC-2S. This is consistent with enhanced site occupancy at higher dye loads and with similar trends reported for rice straw and other ABCs [54], where PSO best describes MB uptake. This indicates chemisorptive control via electron sharing and surface bonding [57]. The observed decrease in PSO rate constants ($k_2$) with increasing MB concentration is indicative of the saturation of high-energy active sites and competitive adsorption. This phenomenon has also been observed in MB adsorption into various ABCs, where Elovich parameters indicate heterogeneous surfaces and varying energetic sites [57,58].

The Avrami exponents $n_{av}$ are typically below unity for most concentrations, indicating a multi-step uptake process involving both rapid surface binding and slower pore penetration. This finding is corroborated by diffusion analyses (Boyd, Weber–Morris, Bangham) that demonstrate intraparticle diffusion contributes to the uptake but is not the sole rate-limiting factor. This observation aligns with the prevailing phenomenon of film and pore diffusion in activated biochar systems, suggesting a multifaceted uptake mechanism [54]. These insights support a mechanism where MB adsorption proceeds through fast external surface interaction, followed by progressive diffusion.

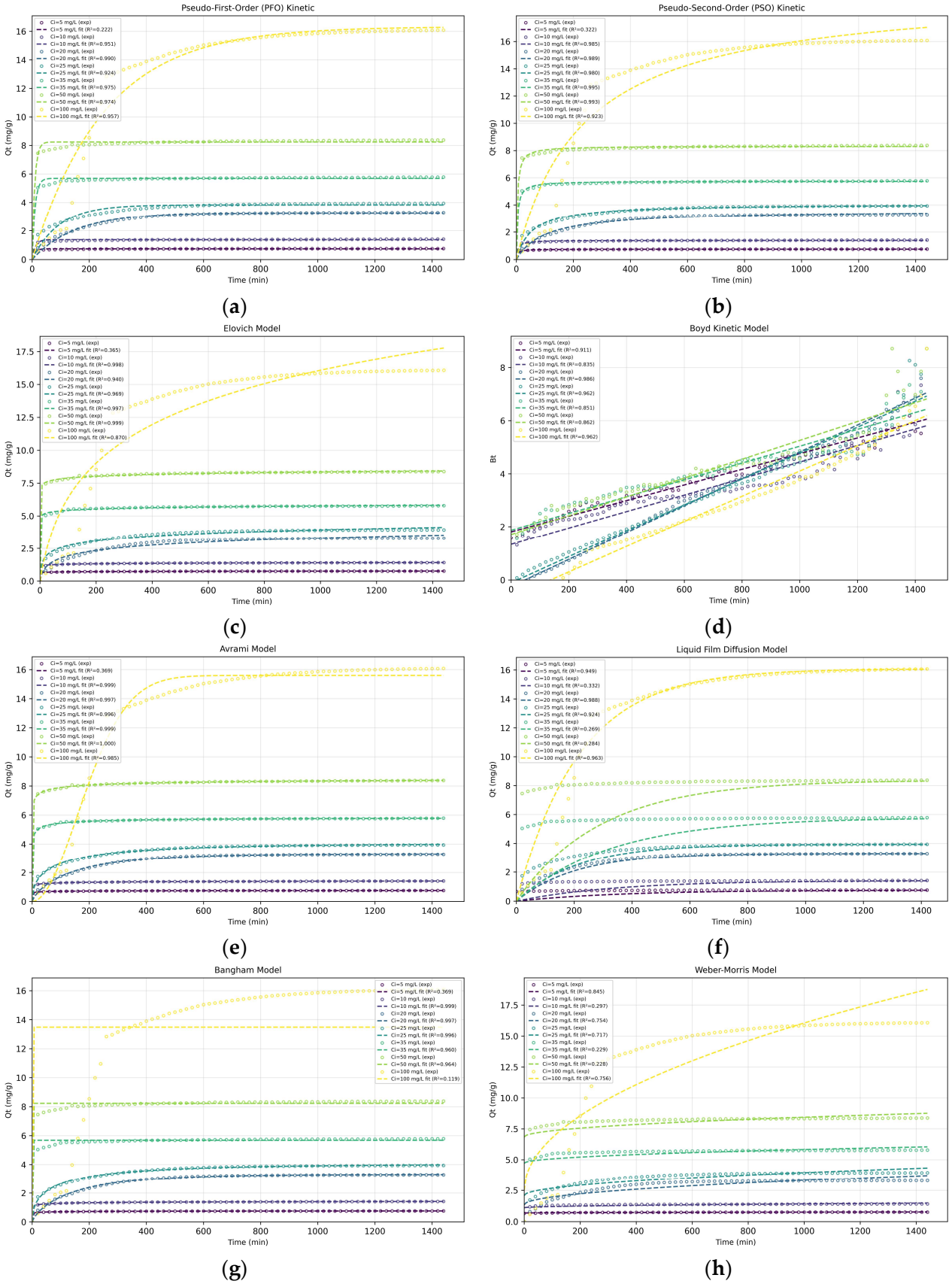



**Figure 6.** Pseudo first order (**a**), Pseudo second order (**b**), Elovich (**c**), Boyd (**d**), Avrami (**e**), Liquid film diffusion (**f**), Bangham (**g**), Weber-Morris (**h**) kinetic curves for the adsorption of MB onto ABC-1S.

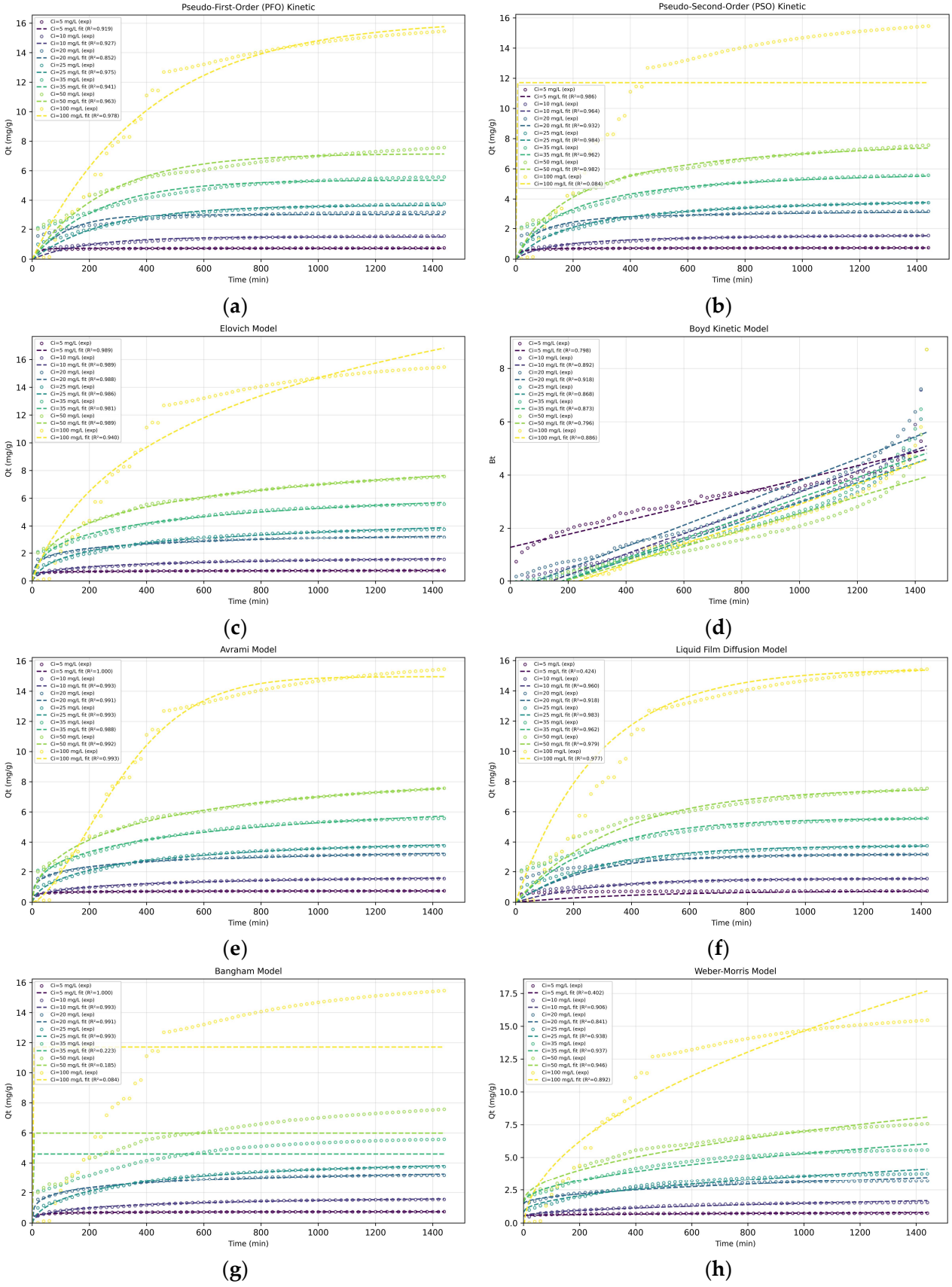



**Figure 7.** Pseudo first order (**a**), Pseudo second order (**b**), Elovich (**c**), Boyd (**d**), Avrami (**e**), Liquid film diffusion (**f**), Bangham (**g**), Weber-Morris (**h**) kinetic curves for the adsorption of MB onto ABC-2S.

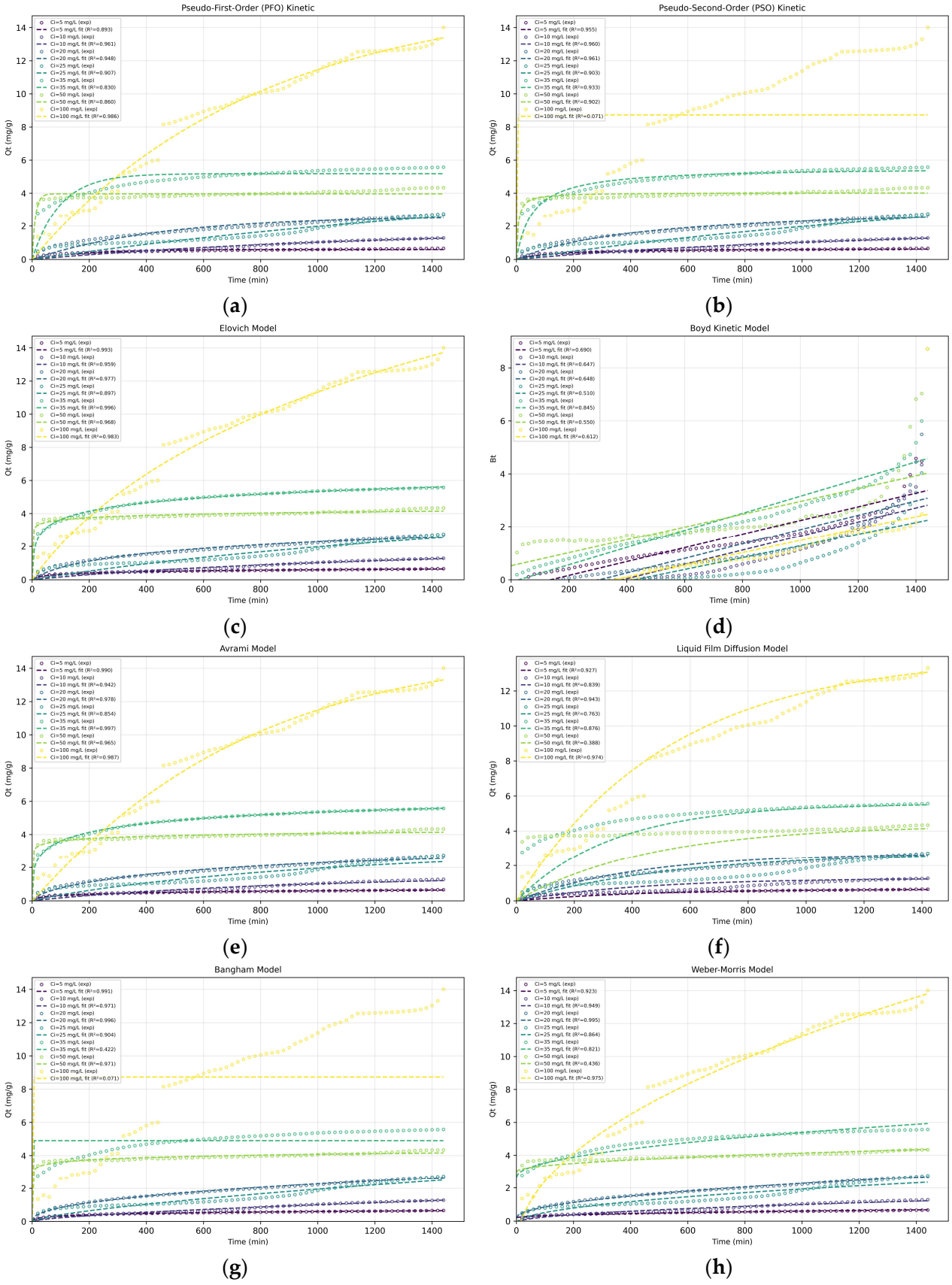



**Figure 8.** Pseudo first order (**a**), Pseudo second order (**b**), Elovich (**c**), Boyd (**d**), Avrami (**e**), Liquid film diffusion (**f**), Bangham (**g**), Weber-Morris (**h**) kinetic curves for the adsorption of MB onto AHTC.

**Table 5.** Kinetic parameters for the adsorption of MB onto ABC-1S.

| Model | Parameter | Initial MB Concentration (mg/L) | | | | | | |
|---|---|---|---|---|---|---|---|---|
| | | **5** | **10** | **20** | **25** | **35** | **50** | **100** |
| PFO | $q_e$ | 0.7418 | 1.3738 | 3.2584 | 3.8280 | 5.6923 | 8.244 | 16.3257 |
| | $k_1$ | 0.1022 | 0.0877 | 0.0066 | 0.0104 | 0.0986 | 0.1089 | 0.0040 |
| | $R^2$ | 0.222 | 0.951 | 0.990 | 0.924 | 0.975 | 0.974 | 0.957 |
| PSO | $q_e$ | 0.7503 | 1.3928 | 3.6139 | 4.0953 | 5.7506 | 8.3218 | 19.7912 |
| | $k_2$ | 0.3178 | 0.1358 | 0.0027 | 0.0045 | 0.0448 | 0.0346 | 0.0002 |
| | $R^2$ | 0.322 | 0.985 | 0.989 | 0.980 | 0.995 | 0.993 | 0.923 |
| Elovich | $\beta$ | 45.72 | 20.5665 | 1.6382 | 1.8890 | 6.9530 | 4.9641 | 0.2096 |
| | $\alpha$ | $1.99 \times 10^{10}$ | $1.513 \times 10^{8}$ | 0.1372 | 0.8932 | $3.68 \times 10^{13}$ | $2.01 \times 10^{14}$ | 0.1341 |
| | $R^2$ | 0.365 | 0.998 | 0.940 | 0.969 | 0.997 | 0.999 | 0.870 |
| Avrami | $q_{av}$ | 0.7906 | 1.4904 | 3.3159 | 4.0516 | 5.8368 | 8.5919 | 15.5990 |
| | $K_{av}$ | 2.8930 | 1.2111 | 0.0067 | 0.0111 | 1.4595 | 4.7658 | 0.0043 |
| | $n_{av}$ | 0.1390 | 0.1437 | 0.7875 | 0.5038 | 0.1988 | 0.1489 | 1.9390 |
| | $R^2$ | 0.369 | 0.999 | 0.997 | 0.996 | 0.999 | 1.000 | 0.985 |
| Boyd | $B_t$ | 0.0029 | 0.0031 | 0.0051 | 0.0049 | 0.0032 | 0.0035 | 0.0048 |
| | $q_e$ | 0.7574 | 1.4126 | 3.2898 | 3.9394 | 5.7851 | 8.3797 | 16.0797 |
| | intercept | 1.8100 | 1.3277 | −0.2440 | −0.1061 | 1.8689 | 1.7097 | −0.6479 |
| | $R^2$ | 0.911 | 0.835 | 0.986 | 0.962 | 0.851 | 0.862 | 0.962 |
| LFD | $K_{lfd}$ | 0.0028 | 0.0029 | 0.0049 | 0.0047 | 0.0030 | 0.0034 | 0.0046 |
| | $q_e$ | 0.7574 | 1.4126 | 3.2898 | 3.9394 | 5.7851 | 8.3797 | 16.0797 |
| | $R^2$ | 0.949 | 0.332 | 0.988 | 0.924 | 0.269 | 0.284 | 0.963 |
| Bangham | $k_B$ | 1.1594 | 1.0279 | 0.0195 | 0.1037 | 5.7851 | 8.3797 | 16.0797 |
| | $n_B$ | 0.1392 | 0.1437 | 0.7875 | 0.5038 | 0.5000 | 0.5000 | 0.5000 |
| | $R^2$ | 0.369 | 0.999 | 0.997 | 0.996 | 0.960 | 0.964 | 0.119 |
| W-M | $k_{wb}$ | 0.0022 | 0.0098 | 0.0624 | 0.0592 | 0.0350 | 0.0500 | 0.4290 |
| | C | 0.6841 | 1.1050 | 1.3385 | 2.0783 | 4.7211 | 6.8448 | 2.4890 |
| | $R^2$ | 0.845 | 0.297 | 0.754 | 0.717 | 0.229 | 0.228 | 0.756 |

**Table 6.** Kinetic parameters for the adsorption of MB onto ABC-2S.

| Model | Parameter | Initial MB Concentration (mg/L) | | | | | | |
|---|---|---|---|---|---|---|---|---|
| | | **5** | **10** | **20** | **25** | **35** | **50** | **100** |
| PFO | $q_e$ | 0.7198 | 1.4795 | 3.0210 | 3.6558 | 5.3603 | 7.1606 | 16.2642 |
| | $k_1$ | 0.0493 | 0.0052 | 0.0082 | 0.0037 | 0.0043 | 0.0038 | 0.0024 |
| | $R^2$ | 0.919 | 0.927 | 0.852 | 0.975 | 0.941 | 0.963 | 0.978 |
| PSO | $q_e$ | 0.7375 | 1.6628 | 3.2723 | 4.3240 | 6.1742 | 8.4646 | 11.7082 |
| | $k_2$ | 0.1247 | 0.0047 | 0.0043 | 0.0010 | 0.0009 | 0.0005 | −76,039.33 |
| | $R^2$ | 0.986 | 0.964 | 0.932 | 0.984 | 0.962 | 0.982 | 0.084 |
| Elovich | $\beta$ | 24.6600 | 3.3659 | 2.1347 | 1.0789 | 0.8370 | 0.5513 | 0.1543 |
| | $\alpha$ | 3264.027 | 0.0430 | 0.3420 | 0.0418 | 0.0970 | 0.0832 | 0.0559 |
| | $R^2$ | 0.989 | 0.989 | 0.988 | 0.986 | 0.981 | 0.989 | 0.940 |
| Avrami | $q_{av}$ | 0.7532 | 1.8654 | 4.0930 | 4.2362 | 7.6073 | 8.9098 | 14.9615 |
| | $K_{av}$ | 0.1033 | 0.0027 | 0.0028 | 0.0026 | 0.0014 | 0.0021 | 0.0028 |
| | $n_{av}$ | 0.2845 | 0.4529 | 0.3242 | 0.6168 | 0.4442 | 0.5593 | 1.5560 |
| | $R^2$ | 1.000 | 0.993 | 0.991 | 0.993 | 0.988 | 0.992 | 0.993 |
| Boyd | $B_t$ | 0.0026 | 0.0039 | 0.0042 | 0.0037 | 0.0038 | 0.0031 | 0.0038 |
| | $q_e$ | 0.7467 | 1.5444 | 3.1842 | 3.7578 | 5.5725 | 7.5693 | 15.4630 |
| | intercept | 1.2615 | −0.5570 | −0.3725 | −0.6849 | −0.6824 | −0.5975 | −0.9023 |
| | $R^2$ | 0.798 | 0.892 | 0.918 | 0.868 | 0.873 | 0.796 | 0.886 |

**Table 6.** *Cont.*

| Model | Parameter | Initial MB Concentration (mg/L) | | | | | | |
|---|---|---|---|---|---|---|---|---|
| | | **5** | **10** | **20** | **25** | **35** | **50** | **100** |
| LFD | $K_{lfd}$ | 0.0023 | 0.0037 | 0.0039 | 0.0034 | 0.0035 | 0.0028 | 0.0035 |
| | $q_e$ | 0.7467 | 1.5444 | 3.1842 | 3.7578 | 5.5725 | 7.5693 | 15.463 |
| | $R^2$ | 0.424 | 0.960 | 0.918 | 0.983 | 0.962 | 0.979 | 0.977 |
| Bangham | $k_B$ | 0.5243 | 0.0694 | 0.1502 | 0.0259 | 5.5725 | 7.5692 | 15.463 |
| | $n_B$ | 0.2845 | 0.4529 | 0.3242 | 0.6168 | 0.5000 | 0.5000 | 0.5000 |
| | $R^2$ | 1.000 | 0.993 | 0.991 | 0.993 | 0.223 | 0.185 | 0.084 |
| W-M | $k_{wb}$ | 0.0063 | 0.0300 | 0.0530 | 0.0868 | 0.1189 | 0.1706 | 0.4819 |
| | C | 0.5465 | 0.5122 | 0.0530 | 0.8152 | 1.5365 | 1.6052 | −0.5945 |
| | $R^2$ | 0.402 | 0.906 | 0.841 | 0.938 | 0.937 | 0.946 | 0.892 |

The kinetics of MB adsorption onto AHTC (Table 7) reflect a mix of surface-controlled mechanisms and mass transfer limits. PSO equilibrium capacities ($q_e$) have been observed to increase with initial MB concentration (e.g., from ~0.668 to ~8.73 mg/g), while decreasing rate constants ($k_2$) have been shown to suggest saturation of high-energy active sites. This is consistent with the findings of studies in which MB kinetics on phosphoric-acid-activated hydrochars fit PSO models indicative of strong surface interactions, including electrostatic attraction and π-π/staking interactions between dye molecules and functional groups introduced during activation [30]. Elovich and Avrami parameters show surface heterogeneity and multi-step adsorption. Diffusion analyses indicate that although intra-particle diffusion contributes, it is not the sole rate-limiting step. Initial uptake is followed by slower pore diffusion into the internal structure [30].

**Table 7.** Kinetic parameters for the adsorption of MB onto AHTC.

| Model | Parameter | Initial MB Concentration (mg $L^{-1}$) | | | | | | |
|---|---|---|---|---|---|---|---|---|
| | | **5** | **10** | **20** | **25** | **35** | **50** | **100** |
| PFO | $q_e$ | 0.5920 | 1.8047 | 2.5866 | 5.1410 | 5.1801 | 3.9640 | 15.9514 |
| | $k_1$ | 0.0054 | 0.0008 | 0.0022 | 0.0004 | 0.0102 | 0.0875 | 0.0012 |
| | $R^2$ | 0.893 | 0.961 | 0.948 | 0.907 | 0.830 | 0.860 | 0.986 |
| PSO | $q_e$ | 0.6678 | 2.7665 | 3.2797 | 7.9558 | 5.5682 | 4.0299 | 8.7255 |
| | $k_2$ | 0.0118 | 0.0002 | 0.0007 | 0.00004 | 0.0031 | 0.0397 | −90,723.56 |
| | $R^2$ | 0.955 | 0.960 | 0.961 | 0.903 | 0.933 | 0.902 | 0.071 |
| Elovich | $\beta$ | 8.1943 | 1.0136 | 1.1777 | 0.3541 | 1.3454 | 4.9797 | 0.1175 |
| | $\alpha$ | 0.0161 | 0.0018 | 0.0115 | 0.0028 | 0.9773 | 128,334 | 0.0237 |
| | $R^2$ | 0.993 | 0.959 | 0.977 | 0.897 | 0.996 | 0.968 | 0.983 |
| Avrami | $q_{av}$ | 0.7946 | 1.5415 | 3.2520 | 3.2978 | 6.6887 | 5.2039 | 15.310 |
| | $K_{av}$ | 0.0021 | 0.0010 | 0.0013 | 0.0008 | 0.0044 | 0.0477 | 0.0013 |
| | $n_{av}$ | 0.4305 | 0.9521 | 0.6513 | 0.9012 | 0.3170 | 0.1087 | 1.0456 |
| | $R^2$ | 0.990 | 0.942 | 0.978 | 0.854 | 0.997 | 0.965 | 0.987 |
| Boyd | $B_t$ | 0.0026 | 0.0027 | 0.0027 | 0.0022 | 0.0032 | 0.0024 | 0.0023 |
| | $q_e$ | 0.6622 | 1.2846 | 2.7100 | 2.7481 | 5.5739 | 4.3366 | 14.0123 |
| | intercept | −0.3542 | −1.0256 | −0.8317 | −0.9445 | −0.0862 | 0.5245 | −0.7994 |
| | $R^2$ | 0.690 | 0.647 | 0.648 | 0.510 | 0.845 | 0.550 | 0.612 |
| LFD | $K_{lfd}$ | 0.0022 | 0.0023 | 0.0024 | −0.9445 | 0.003 | 0.0021 | 0.0019 |
| | $q_e$ | 0.6622 | 1.2846 | 2.7100 | 2.7481 | 5.5739 | 4.3366 | 14.0123 |
| | $R^2$ | 0.927 | 0.839 | 0.943 | 0.763 | 0.876 | 0.388 | 0.974 |
| Bangham | $k_B$ | 0.0739 | 0.0010 | 0.0010 | 0.0010 | 5.5739 | 0.0001 | 14.0123 |
| | $n_B$ | 0.3763 | 0.6573 | 0.4331 | 0.6884 | 0.5000 | 0.0538 | 0.5000 |
| | $R^2$ | 0.991 | 0.971 | 0.996 | 0.904 | 0.422 | 0.971 | 0.071 |
| W-M | $k_{wb}$ | 0.0127 | 0.0349 | 0.0656 | 0.0652 | 0.0861 | 0.0359 | 0.4082 |
| | C | 0.1978 | −0.1016 | 0.1913 | −0.1393 | 2.6613 | 2.9926 | −1.6810 |
| | $R^2$ | 0.923 | 0.949 | 0.995 | 0.864 | 0.821 | 0.436 | 0.975 |

2.2.3. Isotherms Studies

The adsorption data show different mechanisms for MB across the three materials. For ABC-2S (Figure 9), the highest fits ($R^2 \approx 0.977$, lowest RMSE ≈ 0.41) with Freundlich, Figure 9b, Redlich–Peterson, Figure 9c, and Koble–Corrigan, Figure 9f, models are indicative of adsorption on a heterogeneous surface with multilayer and variable energy sites. This finding aligns with recent research that complex isotherm models provide a more accurate description of MB uptake on highly porous and functionally heterogeneous activated carbons (e.g., mesopore-dominant ABCs with superior MB binding) [59]. Conversely, ABC-1S (Figure 10) demonstrates only moderate fits across all models ($R^2 \approx 0.75$), indicating a diminished overall equilibrium affinity and less significant surface heterogeneity, aligning with research indicating that reduced activation development results in inferior adherence to classical isotherms for MB adsorption (e.g., lower $R^2$ and RMSE patterns in base-modified chars) [54].

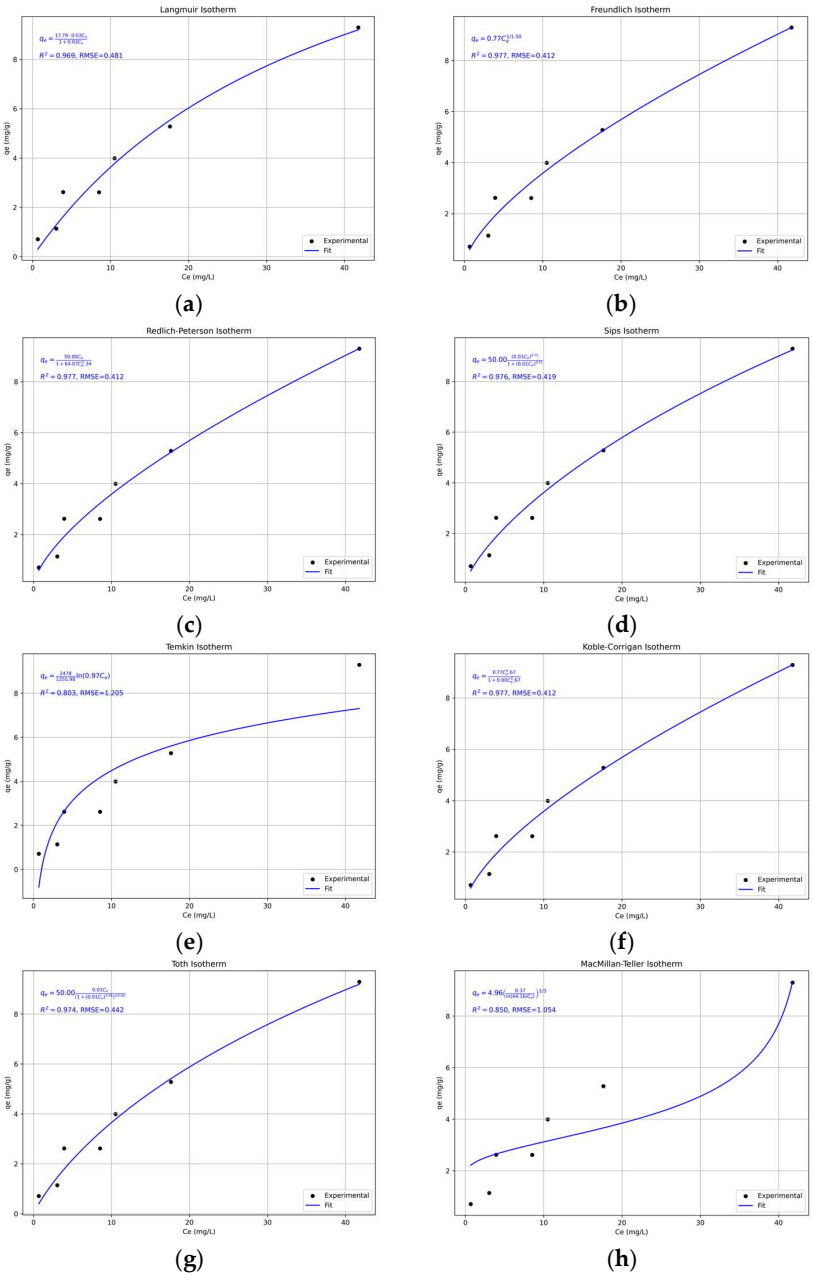



**Figure 9.** Langmuir (**a**), Freundlich (**b**), Redlich-Peterson (**c**), Sips (**d**), Temkin (**e**), Koble-Corrigan (**f**), Toth (**g**), MacMillan-Teller (**h**). Isotherm curves for the adsorption of MB into ABC-2S.

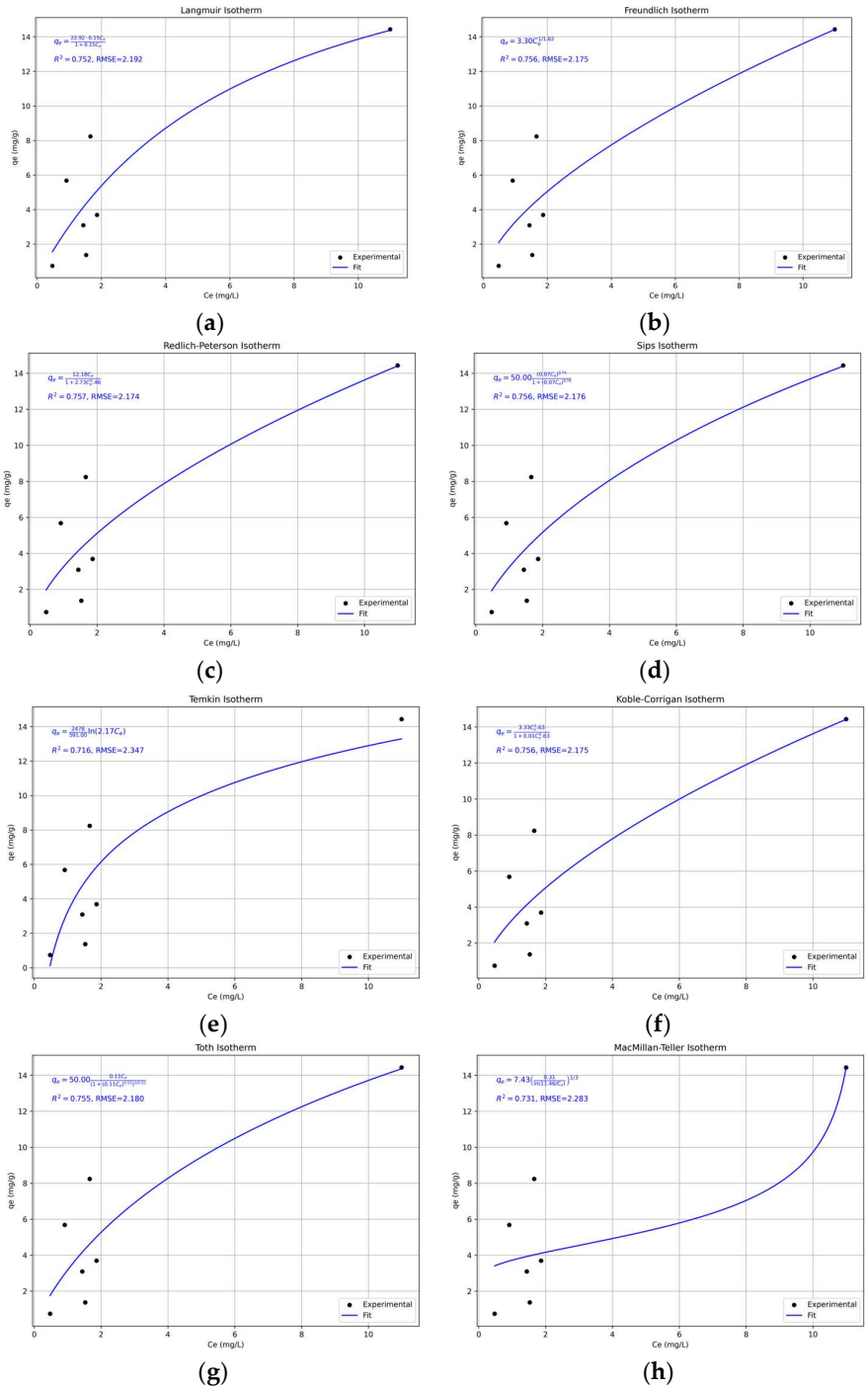



**Figure 10.** Langmuir (**a**), Freundlich (**b**), Redlich-Peterson (**c**), Sips (**d**), Temkin (**e**), Koble-Corrigan (**f**), Toth (**g**), MacMillan-Teller (**h**). Isotherm curves for the adsorption of MB into ABC-1S.

For AHTC (Figure 11), consistently low $R^2$ ($\leq$0.32) and elevated RMSE (>3.4) across models indicate that MB adsorption deviates from conventional Langmuir, Figure 11a, or Freundlich (Figure 11b), models, likely influenced by irregular site interactions and diffusion processes rather than standard monolayer or multilayer equilibrium. This phenomenon is similarly observed in AHTC systems, where surface functionality and pore structure exhibit significant variability, such as AHTC derived from coffee husk, demonstrating mixed kinetics and isotherm behaviour [56]. Collectively, data suggest that KOH-activated materials demonstrate enhanced, heterogeneous MB adsorption, while phosphoric-acid-AHTC exhibits poorly characterized equilibrium behaviour under the examined conditions.

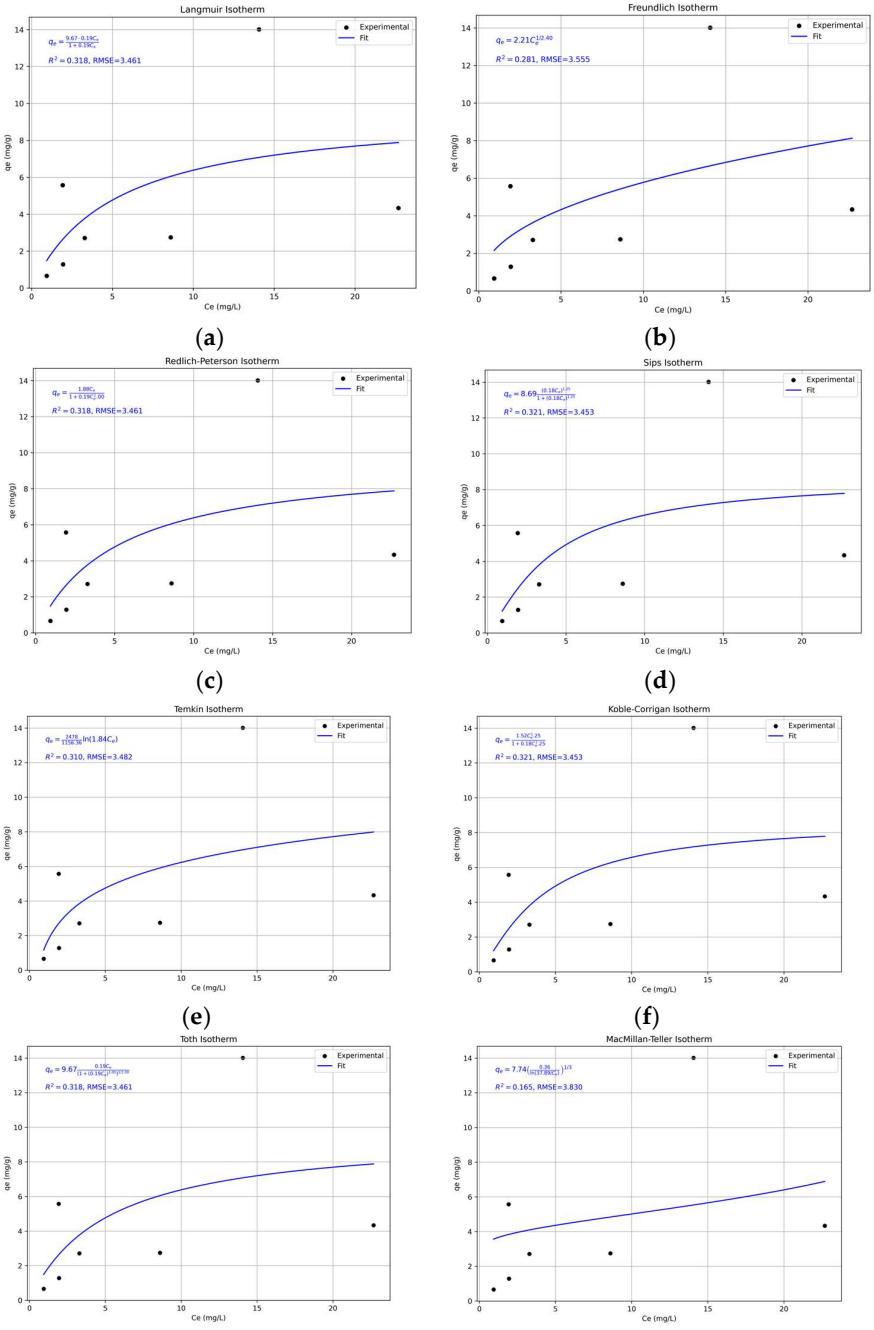



**Figure 11.** Langmuir (**a**), Freundlich (**b**), Redlich-Peterson (**c**), Sips (**d**), Temkin (**e**), Koble-Corrigan (**f**), Toth (**g**), MacMillan-Teller (**h**). Isotherm curves for the adsorption of MB onto AHTC.

The equilibrium adsorption was investigated using various isotherm models (Table 8). The Langmuir model revealed that ABC-1S exhibited the highest monolayer adsorption capacity ($q_1$ = 22.915 mg/g), followed by ABC-2S (17.789 mg/g) and AHTC (9.6704 mg/g). This indicates that KOH-ABCs possess a greater density of accessible adsorption sites than phosphoric-acid- AHTC. This enhancement is commonly ascribed to improved pore development and surface functionality resulting from alkaline activation, as has been reported for ABCs used in dye adsorption applications [21].

**Table 8.** Isotherm Model Fitting Results for MB Adsorption by Adsorbents.

| Model | Parameter | ABC 1-S | ABC-2S | AHTC |
|---|---|---|---|---|
| Langmuir | $q_L$ | 22.915 | 17.789 | 9.6704 |
| | $k_L$ | 0.1532 | 0.0256 | 0.1944 |
| | $R^2$ | 0.752 | 0.969 | 0.318 |
| | RMSE | 2.192 | 0.481 | 3.461 |
| Freundlich | $k_F$ | 3.295 | 0.7709 | 2.2113 |
| | n | 1.6236 | 1.499 | 2.3974 |
| | $R^2$ | 0.756 | 0.977 | 0.281 |
| | RMSE | 2.175 | 0.412 | 3.555 |
| Redlich Peterson | $k_R$ | 12.177 | 50 | 1.8797 |
| | $a_R$ | 2.7281 | 64.07 | 0.1944 |
| | g | 0.4637 | 0.335 | 1 |
| | $R^2$ | 0.757 | 0.977 | 0.318 |
| | RMSE | 2.174 | 0.412 | 3.461 |
| Sips | $q_{max}$ | 50 | 50 | 8.6869 |
| | $K_S$ | 0.0691 | 0.0139 | 0.1755 |
| | n | 0.7365 | 0.7471 | 1.2493 |
| | $R^2$ | 0.756 | 0.976 | 0.321 |
| | RMSE | 2.176 | 0.419 | 3.453 |
| Temkin | $A_T$ | 2.1657 | 0.9722 | 1.8360 |
| | $b_T$ | 591.004 | 1255.98 | 1156.35 |
| | $R^2$ | 0.716 | 0.803 | 0.310 |
| | RMSE | 2.347 | 1.205 | 3.482 |
| Toth | $q_{max}$ | 50 | 50 | 9.6703 |
| | $k_T$ | 0.1061 | 0.0142 | 0.1944 |
| | t | 0.5239 | 0.4897 | 1 |
| | $R^2$ | 0.755 | 0.974 | 0.318 |
| | RMSE | 2.180 | 0.442 | 3.461 |
| Koble Corrigan | A | 3.3253 | 0.7709 | 1.5250 |
| | B | 0.0119 | 0.001 | 0.1755 |
| | n | 0.634 | 0.6671 | 1.2492 |
| | $R^2$ | 0.756 | 0.977 | 0.321 |
| | RMSE | 2.175 | 0.412 | 3.453 |
| MacMillan-Teller | Qs | 7.426 | 4.9591 | 7.7361 |
| | k | 0.3066 | 0.3695 | 0.3629 |
| | Cs | 11.460 | 44.15 | 37.8935 |
| | $R^2$ | 0.731 | 0.850 | 0.165 |
| | RMSE | 2.283 | 1.054 | 3.830 |

Despite exhibiting a lower adsorption capacity, AHTC demonstrated the highest Langmuir affinity constant ($k_1$ = 0.1944 L/mg), indicating stronger adsorbate–adsorbent interactions. This behaviour is indicative of $H_3PO_4$ AHTCs, which characteristically contain a lower number of adsorption sites, albeit those with higher energetic favourability, a consequence of the presence of acidic oxygen-containing functional groups. A similar trend in adsorption has been observed for AHTC derived from biomass waste [56].

Favourable adsorption was confirmed for all materials by the isotherm parameters. Surface properties were indicated as heterogeneous by the range of n values (1.499–2.397). ABC-1S had a higher $k_F$ value (3.295), showing superior performance. Freundlich behaviour is often observed in ABCs and AHTCs made from waste [60].

Three-parameter models like Redlich–Peterson and Sips are applicable when dealing with complex adsorption behaviour involving both homogeneous and heterogeneous

mechanisms. The Redlich–Peterson exponent (g < 1) for ABC-1S and ABC-2S indicates deviation from ideal monolayer adsorption, whereas the Henry constant (g ≈ 1) exhibited Langmuir-type behaviour. The present findings are consistent with those of recent studies, in which hybrid models were required to accurately describe the process of dye adsorption onto chemically ABCs and AHTCs [61,62].

#### 2.2.4. Influence of Wastewater Matrix Complexity

In real wastewater systems, the adsorption behaviour of methylene blue (MB) is strongly influenced by the intrinsic complexity of the aqueous matrix. Industrial effluents rarely contain a single pollutant; instead, they incorporate a diverse combination of organic and inorganic compounds whose relative abundance depends on both the characteristics of the local water supply—such as pH, ionic strength, hardness, salinity, and calcareous origin—and the specific industrial processes involved. These coexisting substances can compete with MB for adsorption sites, interfere with electrostatic interactions, alter pore accessibility, or form surface coatings that reduce the availability of active sites on biochar and hydrochar. Consequently, the removal efficiency observed under ideal single-solute laboratory conditions is often reduced in real matrices. This phenomenon has been widely documented: for example, Li et al. reported that the coexistence of multiple organic and inorganic substances in solution leads to a noticeable decline in dye removal due to competition for adsorption sites and interference from the surrounding medium [63], and similar inhibiting effects have been observed for MB adsorption onto carbon-based adsorbents exposed to complex water compositions [64]. These findings highlight that actual wastewater composition—starting from the baseline characteristics of the water itself and extending to the full suite of process-derived contaminants—has a substantial impact on adsorption performance. Therefore, although the present study elucidates the intrinsic adsorption mechanisms and capacities of the prepared adsorbents under controlled conditions, their behaviour in real industrial effluents may differ. Future work should evaluate these materials in multicomponent or real wastewater systems to quantitatively assess matrix effects and confirm their practical robustness.

### *2.3. Potential for Recovery or Recycling of Adsorbents*

Maintaining an adsorbent's suitability for prolonged application depends largely on its capacity to be regenerated once saturation is reached. Reusing the material across several adsorption–desorption cycles not only reduces the amount of solid waste produced but also allows for the retrieval of the previously retained dye. For the regeneration trials, (Table 9), the MB solution was prepared at a concentration of 35 mg/L, consistent with the value previously identified as representative of typical industrial wastewater. Acetone was chosen as the desorption solvent, and the spent adsorbents were first isolated by filtration and dried at 60 °C for 24 h prior to the recovery procedure [17]. Afterwards, the materials were transferred to a flask containing acetone, continuously stirred for 4 h, filtered again, rinsed with distilled water, and dried once more at 60 °C for 24 h.

**Table 9.** Performance of adsorbents in three adsorption-desorption cycles (after 24 h).

| | **Fresh ABC** | | | **1st Cycle** | | | **2nd Cycle** | | | **3rd Cycle** | | |
|---|---|---|---|---|---|---|---|---|---|---|---|---|
| | **1S** | **2S** | **AHTC** | **1S** | **2S** | **AHTC** | **1S** | **2S** | **AHTC** | **1S** | **2S** | **AHTC** |
| $MB_{removal}$ (%) | 99.8 ± 0.1 | 99.3 ± 0.2 | 99.8 ± 0.1 | 99.8 ± 0.1 | 99.3 ± 0.1 | 99.6 ± 0.1 | 99.7 ± 0.1 | 99.2 ± 0.2 | 99.7 ± 0.2 | 99.7 ± 0.3 | 99.3 ± 0.1 | 99.6 ± 0.2 |
| Qe | 5.81 ± 0.03 | 5.78 ± 0.02 | 5.80 ± 0.01 | 5.81 ± 0.03 | 5.78 ± 0.02 | 5.76 ± 0.01 | 5.80 ± 0.02 | 5.77 ± 0.03 | 5.74 ± 0.01 | 5.80 ± 0.02 | 5.78 ± 0.03 | 5.74 ± 0.01 |

MB removal remained almost 100% consistent across all regeneration cycles, clearly demonstrating the strong reusability of the adsorbents and their capacity to withstand repeated adsorption–desorption steps without structural degradation or loss of performance. The desorbed MB was efficiently recovered through a combined distillation and evaporation process, while both the recovered acetone and the dye exhibited high purity, supporting their potential for recycling and consequently reducing chemical consumption and waste generation. Although the reusability assessment was limited to three cycles, this number is widely adopted in laboratory-scale studies as a practical benchmark for evaluating preliminary adsorbent stability due to the operational and economic costs associated with each regeneration step, including solvent usage, energy demand for drying, and additional processing time. Beyond a certain number of cycles, the marginal scientific benefit of additional testing diminishes relative to these costs, especially at the proof-of-concept stage. Moreover, previous works have shown that three consecutive cycles are sufficient to confirm the short-term robustness of carbonaceous sorbents. For example, porous biochar obtained via KOH activation from bamboo biochar maintained effective MB removal over three cycles, thereby supporting the conclusion that a three-cycle assessment provides a reliable indication of material stability under controlled laboratory conditions [21].

## 3. Materials and Methods

### *3.1. Synthesis and Surface Activation of Carbonaceous Adsorbents*

In this study, AP was processed as follows: biomass was washed, dried, and homogenized to 1–2 mm. For the 1-S route, AP was impregnated with KOH with a KOH-to-biomass ratio of 1:3 (*w*/*w*) and heated in a tube furnace at 20 K/min to 900 °C for 2 h, with a 40 mL/min nitrogen flow. For the 2-S activation, pyrolysis occurred in a tube furnace at 10 °C/min to 900 °C for 1 h under a 40 mL/min nitrogen flow. Afterwards, for the activation step, the biochar sample was impregnated with KOH at a 1:1 (*w*/*w*) ratio. Post-activation, all samples were washed using the same procedure as described elsewhere [17].

In parallel, $H_3PO_4$-assisted hydro-thermal carbonization was performed by mixing biomass with a 25% $H_3PO_4$ solution in a Teflon-lined hydrothermal reactor. Hydrothermal carbonization was performed at 200 °C for 24 h in an oven. The resulting mixture (HTC and resulting liquid phase) was thermally treated, for activation, in a tube furnace at 5 °C/min to 450 °C for 2 h under 40 mL/min nitrogen flow.

Due to the high temperature thermochemical conversion applied during their production, both biochar and hydrochar exhibit intrinsically high chemical stability and negligible leaching potential, as volatile and labile compounds are removed during carbonization, yielding structurally inert carbonaceous solids.

In all activation procedures, the quantities of chemical activating agents were selected based on optimized ratios to ensure effective pore development while minimizing excess reagent use. For the KOH-activated materials, the post-activation treatment incorporated a controlled neutralisation step using nitric acid, which fully converted residual alkaline species into potassium nitrate ($KNO_3$). This compound is non-toxic and widely used as a fertiliser, offering the potential for recovery and valorisation rather than disposal. Following neutralisation, the materials underwent an optimized three-step washing process until the filtrate reached neutral pH, ensuring the complete removal of any remaining activating agent. Similarly, in the case of $H_3PO_4$ activation, the acid was employed in carefully controlled quantities, and the resulting hydrochar was repeatedly washed with deionized water until neutrality was achieved, effectively eliminating free phosphoric acid from the final product. Through these protocols, the presence of environmentally harmful residues was mitigated, and the activation process was aligned with principles of safety and sustainability, demonstrating that the preparation of the adsorbents does not introduce

residual chemical risks and, in the case of KOH, even enables the potential recovery of valuable by-products [65].

### *3.2. Characterization of Biochar and Hydrochar*

Proximate and ultimate analyses of the raw biomass (AP) and the generated substrates (ABC-1S, ABC-2S, HTC) were conducted using an automated elemental analyser (TruSpec Micro, LECO (Saint Joseph, MI, USA)). This technique facilitates the precise determination of carbon (C), hydrogen (H), nitrogen (N), sulfur (S), and oxygen (O) contents in solid or liquid micro-samples, typically requiring approximately 2 mg of sample. Surface functional groups were characterized by ATR-FTIR (Perkin Elmer (Waltham, MA, USA) Spectrum Two, 4000–600 $cm^{-1}$, 4 $cm^{-1}$ resolution, 20 scans) using a diamond ATR accessory. The morphology and microstructure of the samples were examined by SEM (JEOL (Tokyo, Japan) JSM-7000F) [66]. Textural properties, including specific surface area, micropore volume, and average pore width, were determined from nitrogen adsorption/desorption isotherms at −196 °C (Micromeritics ASAP 2010, Norcross, GA, USA). The NLDFT method was applied for pore size distribution calculations. Additionally, porosity and surface characteristics were analysed using the Dubinin–Radushkevich (D–R) method to evaluate micropore volume, adsorption potential, and characteristic adsorption energy, providing insights into the adsorbent performance.

### *3.3. Batch Adsorption Experiments*

Batch adsorption experiments of MB were performed in a quartz vessel with a 10.0 mm optical path at the natural pH of the dye solution (pH = 6.3).

An adsorbent dosage of 6 g/L was added to MB solutions with initial concentrations ranging from 5 to 100 mg MB/L. The suspensions were stirred for 10 s at the beginning of each experiment to guarantee adequate adsorbent-solution interaction. All tests were performed at room temperature, conditions that allowed the sorbent particles to maintain a low settling velocity, remaining predominantly suspended in the solution throughout the 24-h adsorption experiments due to their diminutive and slender particle morphology. The adsorption process was monitored continuously for 24 h using a UV–Vis spectrophotometer (JASCOV (Tokyo, Japan) JASCOV-730) by recording the absorbance at 665 nm. The concentration of MB remaining in solution at each time point was calculated from the measured absorbance using the Beer–Lambert law [67].

The adsorption capacity at a specific time and the removal efficiency were calculated using the following equations [68]. Meanwhile, the quantity of MB adsorbed at equilibrium *Qe* was extracted after the adsorption experiment reached the equilibrium, and time $t_e$ where there is no change in the concentration $C_t$:

$$Q_t = \frac{(C_0 - C_t)V}{m} \quad (1)$$

$$R_t = 100 * \frac{(C_0 - C_t)}{C_0} \quad (2)$$

where $R_t$ was the removal rate (%), and $C_0$, $C_t$ was the initial and $t$-time concentration of MB (mg MB/L). $V$ was the volume of the MB solution (mL), and $m$ was the mass of the adsorbents (g).

### *3.4. Adsorption Modelling*

#### 3.4.1. Response Surface Methodology (RSM) Framework

Response surface methodology (RSM) integrates mathematical and statistical tools to optimize processes by analysing interactions among factors [69]. It investigates experi-

mental input parameters' influence on response parameters and evaluates issues where multiple factors affect the solution's outcome [70].

In this research, a quadratic Central Composite Design (CCD) was employed using Python code (version 3.13) to investigate the interactions between contributing variables on MB adsorption, considering two independent variables: initial MB concentration $C_0$, varied across seven levels, and contact time t. The CCD included factorial runs at the extreme coded levels $(-1, +1)$, center runs replicated at the mid-levels $(0, 0)$ to estimate pure error, and axial (star) runs positioned at $(-\alpha, +\alpha)$ to ensure model rotatability and capture curvature within the design space [71].

The mathematical modelling process entails identifying a function such that:

$$Y = f(x_1, x_2, x_3, \ldots, x_n) \quad (3)$$

where: Y represents the response variable, and $x_1, x_2, x_3, \ldots, x_n$ denote the factors [72].

The response variable (adsorption rate) was modelled as a function of the independent factors using a second-order polynomial. The resulting quadratic model, identified as the optimal predictor by the experimental design, was employed to correlate the variables with the MB removal efficiency Y, given by Equation (4) [73].

$$Y = \beta_0 + \sum_{i=1}^{2} \beta_i X_i + \sum_{2}^{2} \beta_{ii} {X_i}^2 + \sum_{i<j}^{2} \beta_{ij} X_i X_j \quad (4)$$

where $X_i$ is initial concentration $C_0$, $X_j$ is contact time t and the coefficients $\beta_0$, $\beta_i$, $\beta_{ii}$, and $\beta_{ij}$ correspond respectively to the intercept, linear terms, quadratic terms, and interaction terms, It is important to note that these coefficients are not initially known and are instead determined from experimental results. Accordingly, the explicit form of the quadratic model for the two factors, $C_0$ and $t$, is given by:

$$Y = \beta_0 + \beta_1 C_0 + \beta_2 t + \beta_{12} C_0 t + \beta_{11} C_0^2 + \beta_{22} t_0^2 \quad (5)$$

### 3.4.2. Adsorption Kinetics

The adsorption system's kinetics were examined by applying non-linear fitting of several alternative kinetic models in Table 10 using Python. The models applied to the experimental data were evaluated using the coefficient of determination ($R^2$).

**Table 10.** Nonlinear Kinetic Models and their Equations for MB adsorption.

| Model | Equation | Parameter | Mechanism | Reference for the Equation |
|---|---|---|---|---|
| Pseudo first order | $q_t = q_e(1 - e^{-K_1 t})$ | $q_t$: adsorption capacity at time $t$ (mg/g)<br>$q_e$: adsorption capacity at equilibrium (mg/g)<br>$k_1$: pseudo–first–order rate constant ($min^{-1}$)<br>$t$ = contact time (min) | Adsorption is known to occur through a physisorption mechanism, whereby the rate of occupation of adsorption sites is directly proportional to the number of unoccupied sites [74]. | [75] |
| Pseudo Second Order | $q_t = \frac{q_e^2 k_2 t}{1 + q_e k_2 t}$ | $q_t$: adsorption capacity at time $t$ (mg/g)<br>$q_e$: adsorption capacity at equilibrium (mg/g)<br>$k_2$: pseudo second order rate constant ($min^{-1}$) | Each adsorption event occupies one site, consistent with monolayer formation on a finite set of homogeneous sites. Chemisorption is the rate-determining step [21]. | [75] |
| Elovich | $q_t = \frac{1}{\beta} \ln(1 + \alpha\beta t)$ | $\beta$: the quantity of sites available for absorption<br>$\alpha$ : initial adsorption rate (mg/g min) | Adsorption occurs on a highly heterogeneous surface, where the activation energy decreases exponentially with increasing surface coverage [76]. | [53] |
| Avrami | $q_t = q_{av}\left(1 - e^{(K_{av} t)^{n_{av}}}\right)$ | $q_{av}$ : Avrami theoretical value of the amount of the adsorption (mg/g)<br>$K_{av}$: Avrami constant rate<br>$n_{av}$ : Avrami order model | The reaction is located on the surface sites of the solid that are active [77]. | [77] |
| Boyd | $B_t = -0.4977 - \ln\left(1 - \frac{q_t}{q_e}\right)$ | $B_t$ : Boyd constant<br>$q_t$: adsorption capacity at time $t$ (mg/g) | Provides insight into how adsorbates stick. The model can be used to identify the slow step in the process, which is known as the rate-determining step in the adsorbent [78]. | [78] |
| Bangham | $q_t = q_B\left(1 - e^{-k_B t^{n_B}}\right)$ | $k_B$ : Rate constant of adsorption process<br>$n_B$: Constant | Investigates the phase of slow diffusion in the pores of the adsorption process [77]. | [79] |

**Table 10.** *Cont.*

| Model | Equation | Parameter | Mechanism | Reference for the Equation |
|---|---|---|---|---|
| Liquid film diffusion | $L_n\left(1-\frac{q_t}{q_e}\right)=-K_{Lfd}\mathrm{t}$ | $q_t$: adsorption capacity at time $t$ (mg/g)<br>$K_{Lfd}$ : Liquid film Diffusion constant | Adsorption involves the movement of dye ions from the bulk solution to the liquid film surface, influenced by diffusion impediments and determined by external and internal diffusion factors [78]. | [78] |
| Weber-Morris | $q_t=k_{wb}t^{0.5}+C$ | $k_{wb}$: the intra-particle diffusion rate constant (mg/g $\mathrm{min}^{-1/2}$)<br>C: intercept | Intraparticle diffusion is the internal pore-diffusion phase that frequently dictates adsorption kinetics [34]. | [40] |

### 3.4.3. MB Adsorption Isotherms

Adsorption isotherms quantify the equilibrium distribution of adsorbate molecules between the solid surface and the solution [74], offering critical insight into adsorption capacity, surface characteristics, and interaction mechanisms. Although linearized isotherm equations remain common in the literature, their use can introduce substantial errors due to linearization and subjective data selection, leading to inaccurate estimates of adsorption constants and capacities. These limitations are exacerbated for heterogeneous sorbents exhibiting multiple adsorption mechanisms [80]. Consequently, in the present work, nonlinear regression for several isotherm models, which offer a more reliable approach for determining adsorption capacities and affinities, was employed, as summarized in the accompanying table (Table 11), and their corresponding parameters were rigorously evaluated using Python, consistent with the methodology applied in the kinetic analyses.

**Table 11.** Nonlinear Isotherm Models and their Equations for MB adsorption.

| Model | Equation | Parameter | Mechanism | Reference for the Equation |
|---|---|---|---|---|
| Langmuir | $q_e=\frac{q_L K_L C_e}{1+K_L C_e}$ | $q_e$: adsorption capacity at equilibrium (mg/g)<br>$q_L$: Maximum monolayer coverage capacities (mg/g)<br>$k_L$: Langmuir isotherm constant (L/mg)<br>$C_e$ : Equilibrium concentration (mg/L) | There is a fixed number of energetically identical adsorption sites, reversible monolayer adsorption with no further uptake once a site is filled, and no interactions between adsorbed species [80]. | [80] |
| Freundlich | $q_e=K_F(C_e)^{\frac{1}{n}}$ | $q_e$: adsorption capacity at equilibrium (mg/g)<br>$K_F$: Freundlich isotherm constant (mg/g) (L/g)<br>n: Adsorption intensity | Site density decreases exponentially with increasing adsorption heat due to adsorption occurring on sites with varying energy but uniform entropy [77]. | [77] |
| Redlich Peterson | $q_e=\frac{K_R C_e}{1+a_R(C_e)^g}$ | $a_R$ : Redlich–Peterson isotherm constant (L/mg)<br>$C_e$ : Equilibrium concentration (mg/L)<br>g: Redlich–Peterson isotherm exponent<br>$K_R$ : Redlich–Peterson isotherm constant | describes adsorption equilibrium across a wide concentration range in both homogeneous and heterogeneous systems [77]. | [77] |
| Sips | $q_e=\frac{q_{max}K_S(C_e)^n}{1+K_S(C_e)^n}$ | $q_{max}$ : maximum adsorption capacity (mg/g)<br>$C_e$ : Equilibrium concentration (mg/L)<br>$K_S$: Sips isotherm model constant (L/g)<br>n: Sips isotherm model exponent | A hybrid of Langmuir and Freundlich isotherms, describes adsorption on heterogeneous surfaces, reducing limitations at high concentrations [77]. | [81] |
| Temkin | $q_e=\frac{RT}{b_T}\ln(A_T C_e)$ | $A_T$ : Temkin isotherm equilibrium binding constant<br>$b_T$ : Temkin isotherm constant<br>$C_e$ : Equilibrium concentration (mg/L)<br>R: universal gas constant (8.314 J $\mathrm{mol}^{-1}$ $\mathrm{K}^{-1}$)<br>T: temperature (K) | As the coverage of the adsorbent surface increases, with adsorption characterized by a uniform distribution of binding energies, the heat of adsorption for all molecules drops linearly to the highest bond energy [77]. | [77] |
| Toth | $q_e=\frac{q_{max}K_T C_e}{\left(1+(K_T C_e)^t\right)^{\frac{1}{t}}}$ | $q_{max}$: Toth maximum adsorption capacity (mg/g)<br>$C_e$ : Equilibrium concentration (mg/L)<br>$K_T$: Toth isotherm constant (mg/g)<br>t: Toth model exponent | Derived from the Langmuir framework, better fits experimental data by accounting for lateral interactions, surface heterogeneity, and other non-ideal behaviours [77]. | [81,82] |
| Koble Corrigan | $q_e=\frac{A(C_e)^n}{1+B(C_e)^n}$ | A: Koble–Corrigan isotherm constant ($\mathrm{L}^n\mathrm{mg}^{1-n}$ $\mathrm{g}^{-1}$)<br>B: Koble–Corrigan isotherm constant (L/mg)<br>$n$ : Adsorption intensity<br>$C_e$ : Equilibrium concentration (mg/L) | A three-parameter model integrating Langmuir and Freundlich isotherms is applied to heterogeneous adsorption surfaces [77]. | [77] |
| MacMillan-Teller | $q_e=q_s\left(\frac{k}{\ln\left(\frac{C_s}{C_e}\right)}\right)^{\frac{1}{3}}$ | K: MacMillan–Teller isotherm constant<br>$q_s$: theoretical isotherm saturation capacity (mg/g)<br>$C_e$ : Equilibrium concentration (mg/L)<br>$C_s$ : Adsorbate monolayer saturation concentration (mg/L) | The isothermal model has been enhanced by incorporating the effects of surface tension into the Brunauer-Emmett-Teller isotherm [77]. | [77] |

## 4. Conclusions

This study demonstrates the successful conversion of AP into high-performance ABCs through three activation routes: 1-S and 2-S KOH activation at high temperature, and a low-temperature $H_3PO_4$-AHTC. Beyond the sustainable valorisation of agricultural waste, this work introduces a novel computational approach, employing Python-based nonlinear fitting to evaluate kinetic and isotherm models. This method avoids the distortions inherent to linearised equations and enables more accurate interpretation of complex adsorption behaviour; an approach rarely applied in similar studies.

All prepared materials exhibited strong adsorption performance, removing more than 70% of (MB) within the first 8 h at 35 mg/L, using a sorbent dose of 6 g/L, consistent with that applied in the kinetics and equilibrium studies. Across the full concentration range, the KOH-ABCs (ABC-1S and ABC-2S) consistently outperformed the $H_3PO_4$-AHTC, confirming that the activation process effectively enhances pore development and increases the capacity to adsorb higher MB concentrations.

The nonlinear modelling approach revealed that all three adsorbents successfully fitted multiple kinetic and isotherm models, demonstrating their versatile adsorption behaviour. ABC-1S and ABC-2S showed excellent agreement with Avrami and pseudo-second-order kinetics ($R^2$ = 0.996–1.000), indicating chemisorption-dominated, multi-step uptake. AHTC, in contrast, aligned strongly with Elovich and diffusion-controlled models ($R^2 \approx$ 0.993–0.996), reflecting heterogeneous surface interactions. Equilibrium analysis further confirmed these trends, with ABC-1S achieving the highest Langmuir monolayer capacity ($q_1$ = 22.9 mg/g), while AHTC exhibited the strongest Langmuir affinity constant ($k_1$ = 0.194 L/mg), indicating fewer but more energetically favourable sites. A key practical outcome of this work is the excellent regeneration performance of all adsorbents, which retained nearly 100% removal efficiency over multiple cycles when regenerated with a 35 mg/L MB solution. This confirms their robustness and suitability for real-world wastewater treatment applications.

**Author Contributions:** Conceptualization, design, methodology and investigation: all authors; software: A.B.S.; validation, A.B.S., E.C. and M.M.A.; formal analysis, A.B.S. and M.G.A.; data curation, writing—original draft preparation, A.B.S. and E.C.; writing—review and editing, A.B.S., M.M.A. and M.G.A.; project administration, funding acquisition and supervision, M.M.A. and M.G.A. All authors have read and agreed to the published version of the manuscript.

**Funding:** This research was funded by the Gipuzkoa Provincial Government, program "Etorkizuna Eraikiz" 2024/2025 and by the University of the Basque Country (UPV/EHU)'s program for the recruitment of research staff in training (reference PIF24/262).

**Data Availability Statement:** The raw data supporting the conclusions of this article will be made available by the authors on request.

**Conflicts of Interest:** The authors declare no conflicts of interest.

## Abbreviations

The following abbreviations are used in this manuscript:

| | |
|---|---|
| ABC-1S | Activated Biochar 1-step |
| ABC-2S | Activated Biochar 2-step |
| ABCs | Activated biochars |
| AHTC | Activated hydrochar |
| AIC | Akaike Information Criterion |
| ATR-FTIR | Attenuated Total Reflectance Fourier-Transform Infrared Spectroscopy |
| AP | Apple Pruning |
| BC | Biochar |

| | |
|---|---|
| BET | Brunauer-Emmett-Teller |
| BIC | Bayesian Information Criterion |
| CCD | Central Composite Design |
| D–R | Dubinin–Radushkevich |
| HTC | Hydrochar |
| LFD | Liquid film diffusion |
| MB | Methylene blue |
| NLDFT | Non-Local Density Functional Theory |
| PFO | Pseudo First order |
| PSO | Pseudo Second order |
| RMSE | Root Mean Square Error |
| RSM | Response Surface Methodology |
| SEM | Scanning Electron Microscopy |
| UV–Vis | Ultraviolet-Visible |
| W-C | Weber-Moris |

## References


1. Islam, M.M.; Aidid, A.R.; Mohshin, J.N.; Mondal, H.; Ganguli, S.; Chakraborty, A.K. A critical review on textile dye-containing wastewater: Ecotoxicity, health risks, and remediation strategies for environmental safety. *Clean. Chem. Eng.* **2025**, *11*, 100165. [CrossRef]
2. Gurtner, D.; Kresta, M.; Hupfauf, B.; Götz, P.; Nussbaumer, R.; Hofmann, A.; Pfeifer, C. Mechanical strength characterisation of pyrolysis biochar from woody biomass. *Energy* **2023**, *285*, 129366. [CrossRef]
3. Dutta, S.; Adhikary, S.; Bhattacharya, S.; Roy, D.; Chatterjee, S.; Chakraborty, A.; Banerjee, D.; Ganguly, A.; Nanda, S.; Rajak, P. Contamination of textile dyes in aquatic environment: Adverse impacts on aquatic ecosystem and human health, and its management using bioremediation. *J. Environ. Manag.* **2024**, *353*, 120103. [CrossRef] [PubMed]
4. Kavitha, G.; Govindhan, M.; Premkumar, S. Dye pollution and its implications for human health, aquatic ecosystems, and sustainable wastewater treatment: A comprehensive review. *J. Water Process Eng.* **2025**, *80*, 109071. [CrossRef]
5. Kusumlata; Ambade, B.; Kumar, A.; Gautam, S. Sustainable Solutions: Reviewing the Future of Textile Dye Contaminant Removal with Emerging Biological Treatments. *Limnol. Rev.* **2024**, *24*, 126–149. [CrossRef]
6. Al-Tohamy, R.; Ali, S.S.; Li, F.; Okasha, K.M.; Mahmoud, Y.A.-G.; Elsamahy, T.; Jiao, H.; Fu, Y.; Sun, J. A critical review on the treatment of dye-containing wastewater: Ecotoxicological and health concerns of textile dyes and possible remediation approaches for environmental safety. *Ecotoxicol. Environ. Saf.* **2022**, *231*, 113160. [CrossRef]
7. Kumar, M.; Singh, V.P.; Bhat, S.B.; Kumar, R. Environmental risks of textile dyes and photocatalytic materials for sustainable treatment: Current status and future directions. *Discov. Environ.* **2025**, *3*, 132. [CrossRef]
8. Bi, F.; Zhang, B.; Liu, X.; Ma, M.; Hu, Q.; Wang, M.; Wang, L.; Qu, J.; Zhang, Y. Synthesis of polyvinyl chloride modified magnetic hydrochar for effective removal of Pb(II) and bisphenol A from aqueous phase: Performance and mechanism exploration. *Carbon Res.* **2025**, *4*, 13. [CrossRef]
9. Zhang, X.; Chen, F.; Liu, S.; Lou, J.; Liu, W.; Rousseau, D.P.L.; Van Hulle, S. Synthesis, characterization, and methylene blue adsorption isotherms of hydrochars derived from forestry waste and agro-residues. *Biomass Convers. Biorefinery* **2024**, *14*, 1809–1824. [CrossRef]
10. Kundu, S.; Khandaker, T.; Anik, M.A.-A.M.; Hasan, M.K.; Dhar, P.K.; Dutta, S.K.; Latif, M.A.; Hossain, M.S. A comprehensive review of enhanced $CO_2$ capture using activated carbon derived from biomass feedstock. *RSC Adv.* **2024**, *14*, 29693–29736. [CrossRef]
11. Kasemodel, M.C.; de Aguiar, L.G.; Rodrigues, V.G.S.; Romão, É.L. The investigation of the adsorption of methylene blue from water by torrefied biomass. *Colorants* **2025**, *4*, 21. [CrossRef]
12. Singh, R.; Goyal, A.; Sinha, S. Global insights into biochar: Production, sustainable applications, and market dynamics. *Biomass Bioenergy* **2025**, *194*, 107663. [CrossRef]
13. Fan, X.; Wang, S.; Zhang, Y.; Zhao, M.; Zhou, N.; Fan, S. Effect of citric acid modification on the properties of hydrochar and pyrochar and their adsorption performance toward methylene blue: Crucial roles of minerals and oxygen functional groups. *Environ. Monit. Assess.* **2024**, *196*, 664. [CrossRef] [PubMed]
14. Tran, T.H.; Le, A.H.; Pham, T.H.; Duong, L.D.; Nguyen, X.C.; Nadda, A.K.; Chang, S.W.; Chung, W.J.; Nguyen, D.D.; Nguyen, D.T. A sustainable, low-cost carbonaceous hydrochar adsorbent for methylene blue adsorption derived from corncobs. *Environ. Res.* **2022**, *212*, 113178. [CrossRef] [PubMed]

15. Kohzadi, S.; Marzban, N.; Godini, K.; Amini, N.; Maleki, A. Effect of hydrochar modification on the adsorption of methylene blue from aqueous solution: An experimental study followed by intelligent modeling. *Water* **2023**, *15*, 3220. [CrossRef]
16. Li, X.; Bonjour, E.; Jame, P.; Kuzhir, P.; Hurel, C. Production of hydrochar from biomass waste as economical adsorbents for methylene blue—Insight into occurring adsorption phenomena. *Biomass Convers. Biorefinery* **2024**, *14*, 19723–19737. [CrossRef]
17. Antxustegi, M.; Corro, E.; Baloch, M.; Volpe, R.; Gonzalez Alriols, M. Production of activated bio-chars for wastewater treatment: Characterization, activation and evaluation of the adsorption capacity. *Chem. Eng. Trans.* **2022**, *92*, 547–552. [CrossRef]
18. Munzeiwa, W.A.; Tsekoa, P.; Kammies, L.R.D.; Chelechele, K.; Oluwalana-Sanusi, A.E.; Chaukura, N. Influence of biomass baseline potential on biochar properties and performance for targeted applications. *Discov. Water* **2025**, *5*, 77. [CrossRef]
19. Tablas Estadísticas: Producción Agrícola de La C.A. de Euskadi Por Tipo de Cultivo Según Territorio Histórico. 2024. Available online: https://www.eustat.eus/elementos/tbl0012208_c.html (accessed on 17 November 2025).
20. Su, Y.; Fu, W.; Zhang, X.; Wang, X.; Bai, X. Study on the preparation of biochar from Xinjiang biomass pyrolysis and its adsorption characteristics for water pollutants. *Water Air Soil Pollut.* **2025**, *236*, 320. [CrossRef]
21. Ge, Q.; Li, P.; Liu, M.; Xiao, G.-m.; Xiao, Z.-q.; Mao, J.-w.; Gai, X.-k. Removal of methylene blue by porous biochar obtained by KOH activation from bamboo biochar. *Bioresour. Bioprocess.* **2023**, *10*, 51. [CrossRef]
22. Chahal, M.; Kumari, S.; Bhattacharya, A.; Garg, M.C. Evaluating sustainable agricultural waste biomass for methylene blue adsorption in wastewater treatment: A state-of-the-art review. *Bioresour. Technol. Rep.* **2024**, *28*, 101983. [CrossRef]
23. Santos, D.C.B.D.; Evaristo, R.B.W.; Dutra, R.C.; Suarez, P.A.Z.; Silveira, E.A.; Ghesti, G.F. Advancing biochar applications: A review of production processes, analytical methods, decision criteria, and pathways for scalability and certification. *Sustainability* **2025**, *17*, 2685. [CrossRef]
24. Leng, L.; Xu, S.; Liu, R.; Yu, T.; Zhuo, X.; Leng, S.; Xiong, Q.; Huang, H. Nitrogen containing functional groups of biochar: An overview. *Bioresour. Technol.* **2020**, *298*, 122286. [CrossRef] [PubMed]
25. Cai, F.; Li, C.; Yang, C.; Wang, Y.; Zhou, H.; Yang, S.; Tang, J.; Wang, L.; Liu, Y. Preparation of nitrogen-doped bagasse-derived biochar with outstanding methylene blue adsorption performance. *Ind. Crops Prod.* **2024**, *120*, 120415. [CrossRef]
26. Ahmed, M.M.M.; Liao, C.-H.; Venkatesan, S.; Liu, Y.-T.; Tzou, Y.-M.; Jien, S.-H.; Lin, M.-C.; Hsieh, Y.-C.; Osman, A.I. Sulfur-functionalized sawdust biochar for enhanced cadmium adsorption and environmental remediation: A multidisciplinary approach and density functional theory insights. *J. Environ. Manag.* **2025**, *373*, 123586. [CrossRef]
27. Zang, Z.; Chou, S.; Zhao, Q.; Nie, Y.; Xin, M.; Li, Z.; Tian, J.; Li, B. A review of the production and application of mesoporous carbon and its potential as an excellent carrier for the adsorptive delivery of compounds. *Biochar* **2025**, *7*, 44. [CrossRef]
28. Chen, J.; Zhang, L.; Yang, G.; Wang, Q.; Li, R.; Lucia, L.A. Preparation and characterization of activated carbon from hydrochar by phosphoric acid activation and its adsorption performance in prehydrolysis liquor. *BioResources* **2017**, *12*, 5928–5941. [CrossRef]
29. Wang, B.; Zhao, C.; Guo, C. Effect of modifiers on Cr(VI) adsorption performance of modified hydrochars. *Desalination Water Treat.* **2024**, *320*, 100900. [CrossRef]
30. Zhou, F.; Li, K.; Hang, F.; Zhang, Z.; Chen, P.; Wei, L.; Xie, C. Efficient removal of methylene blue by activated hydrochar prepared by hydrothermal carbonization and NaOH activation of sugarcane bagasse. *RSC Adv.* **2022**, *12*, 1885–1896. [CrossRef]
31. Scherdel, C.; Reichenauer, G.; Wiener, M. Relationship between Pore Volumes and Surface Areas Derived from the Evaluation of N2-Sorption Data by DR-, BET- and t-Plot. *Microporous Mesoporous Mater.* **2010**, *132*, 572–575. [CrossRef]
32. Jagiello, J.; Jaroniec, M. 2D-NLDFT Adsorption Models for Porous Oxides with Corrugated Cylindrical Pores. *J. Colloid Interface Sci.* **2018**, *532*, 588–597. [CrossRef]
33. Park, J.H.; Ok, Y.S.; Kim, S.H.; Kang, S.W.; Cho, J.S.; Heo, J.S.; Delaune, R.D.; Seo, D.C. Characteristics of biochars derived from fruit tree pruning wastes and their effects on lead adsorption. *J. Korean Soc. Appl. Biol. Chem.* **2015**, *58*, 751–760. [CrossRef]
34. Mahmood, U.; Alkorbi, A.S.; Hussain, T.; Nazir, A.; Qadir, M.B.; Khaliq, Z.; Faheem, S.; Jalalah, M. Adsorption of lead ions from wastewater using electrospun zeolite/MWCNT nanofibers: Kinetics, thermodynamics and modeling study. *RSC Adv.* **2024**, *14*, 5959–5974. [CrossRef] [PubMed]
35. Elhassan, M.; Kooh, M.R.R.; Chou Chau, Y.-F.; Abdullah, R. Hydrochar from *Shorea* spp.: Sustainable biofuel and methylene blue adsorbent. *Biomass Convers. Biorefinery* **2025**, *15*, 5779–5793. [CrossRef]
36. El-Hendawy, A.N.A. Variation in the FTIR spectra of a biomass under impregnation, carbonization and oxidation conditions. *J. Anal. Appl. Pyrolysis* **2006**, *75*, 159–166. [CrossRef]
37. Liu, X.; Zhou, F.; Shi, C.; Ramirez, J.; Liu, Z.; Hang, F.; Xie, C. Efficient adsorption of methylene blue by polyaminocarboxylated modified hydrochar derived from sugarcane bagasse. *Molecules* **2025**, *30*, 1536. [CrossRef]
38. Wang, T.; Quan, X.; Sun, Z.; Sun, Z. Sustainable biochar synthesis via synergistic $H_2O_2$–KOH modification for enhanced $CO_2$ physisorption. *Carbon Capture Sci. Technol.* **2025**, *15*, 100438. [CrossRef]
39. Ray, A. Characterization of biochars from agricultural byproducts using FTIR spectroscopy and SEM. *Int. J. Agric. Environ. Biotechnol.* **2020**, *13*, 423–430. [CrossRef]
40. Petrović, J.; Mihajlović, M.; Simić, M.; Kalderis, D.; Koprivica, M.; Milojković, J.; Radulović, D. Novel Mg-doped pyro-hydrochars as methylene blue adsorbents: Adsorption behavior and mechanism. *J. Mol. Liq.* **2023**, *376*, 121424. [CrossRef]

41. McCall, M.A.; Watson, J.S.; Tan, J.S.W.; Sephton, M.A. Biochar stability revealed by FTIR and machine learning. *ACS Sustain. Resour. Manag.* **2025**, *2*, 842–852. [CrossRef]
42. Osuna, F.J.; Pavón, E.; Alba, M.D. A technological approach based on engineered nanoclay composites for cesium and iodine retention. *Chemosphere* **2023**, *341*, 140128. [CrossRef] [PubMed]
43. Wu, T.; Lei, J.; Lin, L.; Wang, Q.; Farooq, T.H.; Wang, G.; Wang, J.; Yan, W. MOF-based Ca-alginate/PAA granulate beads for efficient heavy metal removal from water: Synthesis, performance, and mechanism. *Environ. Technol. Innov.* **2023**, *32*, 103428. [CrossRef]
44. Adabala, S.; Dutta, D.P. A review on recent advances in metal chalcogenide-based photocatalysts for $CO_2$ reduction. *J. Environ. Chem. Eng.* **2022**, *10*, 107763. [CrossRef]
45. Liu, P.; Gerometta, M.; Pizzi, A.; Fierro, V. KOH activation mechanism in the preparation of brewer's spent grain-based activated carbons. *Catalysts* **2024**, *14*, 814. [CrossRef]
46. Nandi, R.; Jha, M.K.; Guchhait, S.K.; Sutradhar, D.; Yadav, S. Impact of KOH activation on rice husk derived porous activated carbon for carbon capture at flue-gas-alike temperatures with high $CO_2/N_2$ selectivity. *ACS Omega* **2023**, *8*, 4802–4812. [CrossRef] [PubMed]
47. Jedynak, K.; Charmas, B. Adsorption properties of biochars obtained by KOH activation. *Adsorption* **2023**, *1*, 167–183. [CrossRef]
48. Xu, Z.; Huang, X.; Xu, Y.; Zhang, L.; Cheng, X.; Guo, Q.; He, Y.; Zhang, F. Hierarchically ordered carbon tube-sheet superstructure via template-directed self-assembly of polyimide. *Chem. Eng. J.* **2019**, *364*, 201–207. [CrossRef]
49. de Araujo, L.G.; Martins, G.F.; Campera, A.A.A.; Marumo, J.T.; Guilhen, S.N. Biosorption of methylene blue by bone meal: Experimental and machine learning modeling. *Front. Environ. Chem.* **2024**, *5*, 1451051. [CrossRef]
50. Wang, Y.; Song, X.; Xia, S.; Wu, T.; Huang, M.; Karatum, O.; Pidko, E. Guideline for modeling solid-liquid adsorption: Kinetics, isotherm, fixed bed, and thermodynamics. *Chemosphere* **2024**, *349*, 140736. [CrossRef]
51. Allouss, D.; Essamlali, Y.; Amadine, O.; Chakir, A.; Zahouily, M. Response surface methodology for optimization of methylene blue adsorption onto carboxymethyl-cellulose-based hydrogel beads. *RSC Adv.* **2019**, *9*, 37858–37869. [CrossRef]
52. Habibu, S.; Ladan, M.; Safana, A.A.; Dandalma, Z.A.; Saleh, I.; Abdullahi, S.R. Optimization of methylene blue adsorption onto activated carbon derived from pineapple peel waste using response surface methodology. *UMYU Sci.* **2023**, *2*, 45–55. [CrossRef]
53. Wei, F.; Jin, S.; Yao, C.; Wang, T.; Zhu, S.; Ma, Y.; Qiao, H.; Shan, L.; Wang, R.; Lian, X.; et al. Revealing the Combined Effect of Active Sites and Intra-Particle Diffusion on Adsorption Mechanism of Methylene Blue on Activated Red-Pulp Pomelo Peel Biochar. *Molecules* **2023**, *28*. [CrossRef] [PubMed]
54. Senapati, S.; Giri, J.; Mallick, L.; Singha, D.; Bastia, T.K.; Rath, P.; Rana, M.K.; Panda, A.K. Rapid adsorption of industrial cationic dye pollutant using base-activated rice straw biochar: Performance, isotherm, kinetic and thermodynamic evaluation. *Discov. Sustain.* **2025**, *6*, 46. [CrossRef]
55. Gonçalves dos Santos, M.; Destefani Paquini, L.; Leite Quintela, P.H.; Roberto Profeti, L.P.; Guimarães, D. Insights into kinetics and thermodynamics for adsorption methylene blue using ecofriendly zeolites materials. *ACS Omega* **2025**, *10*, 20326–20340. [CrossRef]
56. Tran, T.H.; Le, A.H.; Pham, T.H.; Duong, L.D.; Nguyen, X.C.; Nadda, A.K.; Chang, S.W.; Chung, W.J.; Nguyen, D.D.; Nguyen, D.T. Adsorption isotherms and kinetic modeling of methylene blue dye onto a carbonaceous hydrochar adsorbent derived from coffee husk waste. *Sci. Total Environ.* **2020**, *725*, 138325. [CrossRef]
57. Pieczykolan, B. Investigation of adsorption kinetics and isotherms of synthetic dyes on biochar derived from post-coagulation sludge. *Int. J. Mol. Sci.* **2025**, *26*, 7912. [CrossRef]
58. Ben Ali, M.; Flayou, M.; Boutarba, Y.; El Youssfi, M.; Bakhtaoui, Y.; El Hazzat, M.; Sifou, A.; Dahhou, M.; Kacimi, M.; Benzaouak, A.; et al. Conversion of Urban Sludge into KOH-Activated Biochar for Methylene Blue Adsorption. *Moroc. J. Chem.* **2024**, *12*, 1852–1869. [CrossRef]
59. Wang, L.; Zhou, Z.; Li, X.; Zeng, L.; Xu, W.; Ma, Y.; Cai, J. Enhanced removal of methylene blue from water by mesopore-dominant biochar from kelp: Kinetic, equilibrium and thermodynamic studies. *Colloids Surf. A Physicochem. Eng. Asp.* **2024**, *688*, 133652. [CrossRef]
60. Fito, J.; Abewaa, M.; Mengistu, A.; Angassa, K.; Ambaye, A.D.; Moyo, W.; Nkambule, T. Adsorption of methylene blue from textile industrial wastewater using activated carbon developed from Rumex abyssinicus plant. *Sci. Rep.* **2023**, *13*, 5427. [CrossRef]
61. Kalam, S.; Abu-Khamsin, S.A.; Kamal, M.S.; Patil, S. Surfactant adsorption isotherms: A review. *ACS Omega* **2021**, *6*, 32342–32360. [CrossRef]
62. Danso-Boateng, E.; Fitzsimmons, M.; Ross, A.B.; Mariner, T. Response Surface Modelling of Methylene Blue Adsorption onto Seaweed, Coconut Shell and Oak Wood Hydrochars. *Water* **2023**, *15*, 977. [CrossRef]
63. Wang, S.; Zheng, Q.; Liu, Y.; Ze, Y.; Wang, Y.; Wu, Y.; Qi, J.; Qu, J.; Zhang, Y. Co-Incorporation of Nitrogen and Boron into Microscale Zero-Valent Iron via Mechanochemical Ball-Milling Method Improved Cr(VI) Elimination: Performance and Mechanism Investigation. *Chem. Eng. J.* **2025**, *506*, 160050. [CrossRef]

64. Salahshoori, I.; Wang, Q.; Nobre, M.A.L.; Mohammadi, A.H.; Dawi, E.A.; Khonakdar, H.A. Molecular Simulation-Based Insights into Dye Pollutant Adsorption: A Perspective Review. *Adv. Colloid Interface Sci.* **2024**, *333*, 103281. [CrossRef] [PubMed]
65. Menya, E.; Olupot, P.W.; Storz, H.; Lubwama, M.; Kiros, Y. Production and performance of activated carbon from rice husks for removal of natural organic matter from water: A review. *Chem. Eng. Res. Des.* **2018**, *129*, 271–296. [CrossRef]
66. Shadangi, K.P.; Sarangi, P.K.; Behera, A.K. Characterization techniques of biomass: Physico-chemical, elemental, and biological. In *Bioenergy Engineering: Fundamentals, Methods, Modelling, and Applications*; Elsevier: Amsterdam, The Netherlands, 2023; pp. 51–66. [CrossRef]
67. Mayerhöfer, T.G.; Pahlow, S.; Popp, J. The Bouguer–Beer–Lambert law: Shining light on the obscure. *ChemPhysChem* **2020**, *21*, 2029–2046. [CrossRef]
68. Li, H.; Budarin, V.L.; Clark, J.H.; North, M.; Wu, X. Rapid and efficient adsorption of methylene blue dye from aqueous solution by hierarchically porous, activated starbons®: Mechanism and porosity dependence. *J. Hazard. Mater.* **2022**, *436*, 129174. [CrossRef]
69. Halici, Z.; Demirhan, E. Response surface methodology for optimizing adsorption process parameters for tadalafil removal by raw eggshell. *Biomass Convers. Biorefinery* **2025**, *15*, 6027–6036. [CrossRef]
70. Nagarajan, T.; Krithiga, A.; Abdulrahman, N.; Alhaji, A.; Olisa, M.; Akomolafe, S.; Busari, I. Adsorption parameters optimization of spent coffee ground biochar for methylene blue removal using response surface methodology. *Chemosphere* **2024**, *364*, 143242. [CrossRef]
71. Mohan, C.; Bashir, M.; Annachhatre, A.; Dikshit, A.K. Response surface modelling and optimization for copper removal using oxidized pine-needle biochar. *AQUA Water Infrastruct. Ecosyst. Soc.* **2024**, *73*, 1698–1724. [CrossRef]
72. Nouaa, S.; Aziam, R.; Benhiti, R.; Carja, G.; Zerbet, M.; Chiban, M. Exploiting RSM and ANN modeling methods to optimize phosphate ions removal using LDH/alginate composite beads. *J. Water Process Eng.* **2024**, *68*, 106333. [CrossRef]
73. Obayomi, K.S.; Oni, A.O.; Adeyi, A.O.; Adekola, F.A.; Fanida, J.A.; Alabi, A.O. A response surface methodology approach for the removal of methylene blue dye from wastewater using sustainable and cost-effective adsorbent. *Process Saf. Environ. Prot.* **2024**, *184*, 129–150. [CrossRef]
74. Hassaan, M.A.; Yılmaz, M.; Helal, M.; El-Nemr, M.A.; Ragab, S.; El Nemr, A. Isotherm and kinetic investigations of sawdust-based biochar modified by ammonia to remove methylene blue from water. *Sci. Rep.* **2023**, *13*, 39971. [CrossRef]
75. Consiglio Kasemodel, M.; Romão, É.L.; Papa, T.B.R. Adsorption of methylene blue on Orbignya speciosa (babassu) mesocarp commercial biochar. *Int. J. Environ. Sci. Technol.* **2024**, *21*, 1671–1682. [CrossRef]
76. Gole, P.; Raut, K.; Kandasubramanian, B. Polymer-based biochar materials for environmental remediation: A review. *Hybrid Adv.* **2024**, *6*, 100267. [CrossRef]
77. Benjelloun, M.; Miyah, Y.; Akdemir Evrendilek, G.; Zerrouq, F.; Lairini, S. Recent advances in adsorption kinetic models: Their application to dye types. *Arab. J. Chem.* **2021**, *14*, 103031. [CrossRef]
78. Oguanobi, N.C.; Onu, C.E.; Onukwuli, O.D.; Anike, E.N.; Ude, C.N. Modeling and kinetics investigation of adsorptive properties and regeneration of modified clay on azo dyes removal from aqueous solution using artificial intelligence (ANN, ANFIS) and RSM. *Nat. Sci.* **2025**, *43*, 316–339. [CrossRef]
79. Tsiotsias, A.I.; Georgiadis, A.G.; Charisiou, N.D.; Goula, M.A. $CO_2$ physisorption over an industrial molecular sieve zeolite: An experimental and theoretical approach. *Materials* **2023**, *16*, 6656. [CrossRef]
80. Vitek, R.; Masini, J.C. Nonlinear regression for treating adsorption isotherm data to characterize new sorbents: Advantages over linearization demonstrated with simulated and experimental data. *Heliyon* **2023**, *9*, e15128. [CrossRef]
81. Mosoarca, G.; Vancea, C.; Popa, S.; Dan, M.; Boran, S. Modelling and optimization of methylene blue adsorption process on *Leonurus cardiaca* L. biomass powder. *Processes* **2023**, *11*, 3385. [CrossRef]
82. El Nemr, A.; El-Sikaily, A.; Khaled, A. Modeling of adsorption isotherms of Methylene Blue onto rice husk activated carbon EJAR. *Egypt. J. Aquat. Res.* **2010**, *36*, 403–425.


**Disclaimer/Publisher's Note:** The statements, opinions and data contained in all publications are solely those of the individual author(s) and contributor(s) and not of MDPI and/or the editor(s). MDPI and/or the editor(s) disclaim responsibility for any injury to people or property resulting from any ideas, methods, instructions or products referred to in the content.